Development of filtered Euler–Euler two-phase model for circulating fluidised bed: High resolution simulation, formulation and a priori analyses

Ali Özel, Pascal Fede, Olivier Simonin

Development of filtered Euler–Euler two-phase model for circulating fluidised bed: High resolution simulation, formulation and *a priori* analyses

A. Ozel *, P. Fede, O. Simonin

Université de Toulouse, INPT, UPS, IMFT, Allée Camille Soula, F-31400 Toulouse, France
CNRS, Institut de Mécanique des Fluides de Toulouse, F-31400 Toulouse, France

Keywords:
Euler–Euler two-phase model
Periodic circulating fluidised bed
Filtering approach
Sub-grid modelling

A B S T R A C T

Euler–Euler two-phase model simulations are usually performed with mesh sizes larger than the small-scale structure size of gas–solid flows in industrial fluidised beds because of computational resource limitation. Thus, these simulations do not fully account for the particle segregation effect at the small scale and this causes poor prediction of bed hydrodynamics. An appropriate modelling approach accounting for the influence of unresolved structures needs to be proposed for practical simulations. For this purpose, computational grids are refined to a cell size of a few particle diameters to obtain mesh-independent results requiring up to 17 million cells in a 3D periodic circulating fluidised bed. These mesh-independent results are filtered by volume averaging and used to perform *a priori* analyses on the filtered phase balance equations. Results show that filtered momentum equations can be used for practical simulations but must take account of a drift velocity due to the sub-grid correlation between the local fluid velocity and the local particle volume fraction, and particle sub-grid stresses due to the filtering of the non-linear convection term. This paper proposes models for sub-grid drift velocity and particle sub-grid stresses and assesses these models by *a priori* tests.

1. Introduction

Gas–solid reacting circulating fluidised beds are used in many industrial applications such as fluid catalytic cracking (FCC) in petroleum refineries, and biomass pyrolysis or fossil combustion in power plants. Correct prediction of the hydrodynamic characteristics of gas–solid flows is crucial to improve performance and design of reactors and satisfy safety requirements. For such flows in large scale of circulating fluidised beds (CFBs), an Euler–Euler two-phase (two-fluid) model is commonly used to model the hydrodynamics of beds (van der Hoef et al., 2008).

In Euler–Euler two-phase models, the phases are treated as interpenetrating continua, which means that separate transport equations of mass, momentum and energy for each phase have to be solved. Unknown terms, such as velocity correlations or interaction terms between fluid and solid phases, are accounted for using constitutive laws. For a particulate phase, the constitutive laws can be derived within the framework of the Kinetic Theory of Granular Flow (KTGF) (for reviews, see Gidaspow et al., 2004; van der Hoef et al., 2008). However, an Euler–Euler two-phase model using a mesh size larger than small-scale structure size fails to predict the hydrodynamic characteristics of industrial applications (Sundaresan, 2000; Wang, 2009). Several authors have investigated the failures of the Euler–Euler two-phase model (O'Brien and Syamlal, 1993; Agrawal et al., 2001; Yang et al., 2003; Heynderickx et al., 2004; Andrews et al., 2005; Igci et al., 2008; Wang, 2009; Parmentier et al., 2008). It has been shown that the existence of meso-scale structures, such as streamers and clusters, can have dramatic effects on the overall dynamic behaviours and they are cancelled out by simulations using mesh sizes larger than meso-scale structure size. The meso-scale structures have also been well established by some experimental studies. Weinstein et al. (1984) study on high-velocity gas–solid flow in a vertical pipe points out that there are particle segregations over the cross section. The size of the meso-scale structures are typically of the order of 10–100 particle diameters and they accumulate near riser walls and, in some cases, a large region of high concentration exists in the centre of a riser (Weinstein et al., 1984; Gidaspow, 1994). These structures continuously occur in risers because of local instabilities due to the damping of particle random motion by the interstitial gas and inelastic collisions (Agrawal et al., 2001) or the non-linear dependence of the two-phase momentum coupling on the solid volume fraction through the gas pressure gradient or the drag force

* Corresponding author at: Université de Toulouse, INPT, UPS, IMFT, Allée Camille Soula, F-31400 Toulouse, France.

E-mail addresses: ali.ozel@imft.fr (A. Ozel), pascal.fede@imft.fr (P. Fede), olivier.simonin@imft.fr (O. Simonin).

correlation. The formation and breakage of meso-scale structures can be captured by an Euler–Euler two-phase model on a small domain. However, in large industrial units, these structures cannot be fully resolved due to the computational cost. The influence of the mesh resolution on the macroscopic behaviour in circulating and dense fluidised beds has been studied by several authors. Agrawal et al. (2001) showed that if the mesh resolution is not sufficient to predict all temporal–spatial structures in a fully periodic domain, the drag force is overestimated. Parmentier et al. (2008) showed that particle volume fraction predicted by very-coarse-mesh numerical simulation of Geldart A particles in a 2D dense fluidised bed was nearly homogeneous. Wang et al. (2009) performed highly resolved three-dimensional simulations of a bubbling fluidised bed at moderate superficial gas velocity. They concluded that the prediction of bed height by Lagrangian simulation was in a good agreement with that of the standard two-fluid model when mesh resolution was sufficient.

Wang (2009) reviews constitutive laws to overcome the failure of Euler–Euler model predictions for the hydrodynamics of large-scale gas-fluidised beds of Geldart A particles. It is stated that almost all of the studies concentrated on the drag force. Almost two decades ago, O'Brien and Syamlal (1993) and Boemer et al. (1994) pointed out the need to have closure for the drag coefficient in order to account for the effect of unresolved clusters. The correlation of O'Brien and Syamlal (1993) obtained from an air-FCC system with specific solid circulation fluxes gives reasonably good predictions for some specific cases. McKeen and Pugsley (2003) suggested using a scale factor between 0.2 and 0.3 for the drag law to account for small structure effects on the global hydrodynamics of a freely bubbling bed. Hosseini et al. (2009) proposed a scale factor of 0.1. Gao et al. (2008) used a scale factor set at 0.04 for their numerical simulations.

Recently, the EMMS method developed by Li and Kwauk (1994) has been used to predict steady flows inside circulating fluidised beds. The EMMS method assumes that particles move in clusters through a dilute phase composed of the surrounding gas and a few randomly distributed particles. It was integrated into the Eulerian formalism in the form of a drag correction (Wang and Li, 2007).

In addition to these approaches, Agrawal et al. (2001) have shown that the effect of meso-scale structures on the macroscopic behaviour for practical simulations can be taken into account by sub-grid scales through additional closure relations, which can be derived by using a highly resolved simulation. Andrews et al. (2005) proposed a deterministic and stochastic effective drag coefficient for the simulation of a large-scale circulating fluidised bed on a grid having a resolution that was relatively coarse compared to the small-scale structure size. Their effective drag coefficient was measured using the highly resolved simulations of periodic flows obtained by Agrawal et al. (2001) and depended on the particle volume fraction. Following this study, Igci et al. (2008) and Igci and Sundaresan (2011) proposed models for the effective drag coefficient, the filtered particle phase pressure, and the filtered particle phase viscosity. Igci et al. (2012) then validated numerical simulations using the proposed models with experimental data.

In the present paper, we perform detailed numerical simulations of locally instantaneous phase equations in the framework of an Euler–Euler approach for a 3D periodic circulating fluidised bed in order to study the influence of unresolved structures on drag force and particulate phase stresses. We demonstrate that the overestimation of the filtered drag is linked to the existence of a sub-grid drift velocity that should be taken into account as pointed out by Parmentier et al. (2012) for a 2D dense fluidised bed. We propose functional and structural models constructed for sub-grid drift velocity. Additionally, we propose closures for particulate phase sub-grid stresses like those derived for single-phase compressible turbulent flows. We test the predictability of the models with *a priori* tests.

The paper is organised as follows. In Section 2, we introduce the flow configuration, a 3D periodic circulating fluidised bed (PCFB) where the mean gas–solid flow is periodically driven in the opposite direction to gravity, and we review the previous works on vertical riser flows. We demonstrate the mesh dependency of time-domain averaged statistical quantities such as the mean relative velocity, solid mass flux, and particle agitation (granular temperature) and discuss the mesh-independent results. Mesh-independent results obtained in Section 2 are used for budget analyses of filtered particle momentum and agitation equations. The effects of additional terms due to the filtering procedure are investigated in Sections , 3, and 4. After this, we carry out *a priori* tests on the sub-grid contribution of drag force and sub-grid scale (SGS) stress tensor of the particulate phase. In Sections 5 and 6, models for the sub-grid drag contribution and SGS stress tensor are proposed and several model coefficients are calculated from mesh-independent results. The present study aims to identify sub-grid contributions due to the filtering approach, then validate the modelling of these terms by means of *a priori* tests.

2. Mesh-independent result

Gas–particle flows were simulated in a 3D PCFB by using the Euler–Euler model formalism based on separate mean transport equations of mass, momentum and energy for gas and particulate phases. In Appendix A, we present the mathematical modelling of gas–solid flow. For the momentum transfer between the gas and particulate phase, we consider only the drag and the buoyancy forces. The computational domain is shown by Fig. 1. For all the cases presented in the paper, the initial velocity field for both phases is set to zero and the initial solid volume fraction is taken to be uniformly equal to 5%. The flow is driven in the direction opposite to gravity by a uniform vertical pressure gradient. Similarly to Agrawal et al. (2001), we write the gas pressure term in Eq. (A.2) as

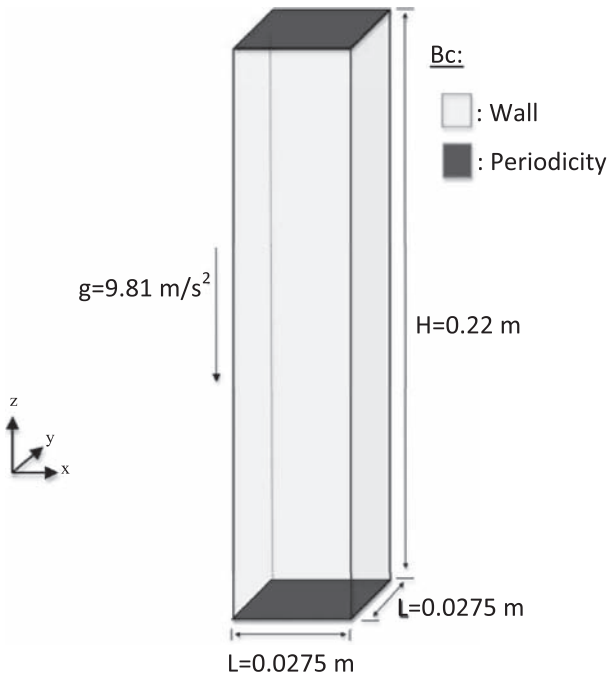

Fig. 1. Periodic circulating fluidized bed (PCFB).

$$P_g(\mathbf{x},t) = (z - z_0)\Delta P(t) + P_g''(\mathbf{x},t) \quad (1)$$

The first term on the right-hand side represents the mean vertical pressure drop due to the total mass of a two-phase mixture (hydrostatic part) and the momentum loss through wall friction (no-slip boundary condition for the gas phase). The second term on the right-hand side is the computed gas pressure, which obeys the periodic boundary conditions. Agrawal et al. (2001) tested three different choices of boundary condition for the particulate phase: no-slip, free-slip and partial slip (defined by a particle–wall coefficient of restitution and a specularity coefficient) and showed that the meso-scale structures occurred with all types of boundary conditions. We chose to impose a free-slip condition representing elastic bouncing of frictionless particles on a smooth wall. For the reference case, particles (d_p = 75 μm and ρ_p = 1500 kg/m^3) interact with air at standard conditions (ρ_g = 1.186 kg/m^3 and $\mu_g = 1.8 \times 10^{-5}$ Pa s). The normal restitution coefficient e_c is set to 0.9.

Agrawal et al. (2001) stated that statistical quantities over the whole domain were strongly dependent on the mesh size but became mesh-independent when mesh size was of the order of a few particle diameters. In this work, a mesh refinement study is carried out to ensure that the mesh resolution is sufficient and all spatial and temporal scales of solid and gas phases are captured. Fig. 2 shows instantaneous particle volume fraction fields in the PCFB obtained by different mesh resolutions. As the mesh resolution increases, inhomogeneous structures are better resolved. For the reference case, the coarsest mesh consists of approximately 110,000 cells ($24 \times 24 \times 192$, $\Delta x = \Delta y = \Delta z = 1.145 \times 10^{-3}$ m with inverse Froude number $Fr_\Delta^{-1} = 0.175$) and the finest mesh consists of approximately 17 million cells ($128 \times 128 \times 1024$, $\Delta x = \Delta y = \Delta z = 0.215 \times 10^{-3}$ m with inverse Froude number $Fr_\Delta^{-1} = 0.032$). As in previous studies (Agrawal et al., 2001; Igci et al., 2008; Parmentier et al., 2012), the effect of the mesh size is analysed with respect to the Froude number Fr_Δ defined as

$$Fr_\Delta = \frac{\left(\tau_p^{St}\right)^2 |\mathbf{g}|}{\Delta} \quad (2)$$

where the Stokes relaxation time τ_p^{St} is given by $\frac{\rho_p}{\rho_g}\frac{d_p^2}{18\nu_g}$ and $|\mathbf{g}|$ is the norm of the gravity acceleration. The characteristic velocity $\tau_p^{St}|\mathbf{g}|$ is equal to 0.255 m/s and the characteristic length scale $\left(\tau_p^{St}\right)^2|\mathbf{g}|$ is 0.0066 m approximately 3% of the column height, which ensures no effect of the periodic boundary condition on the results (see Table 1).

To investigate the dynamic behaviour of particles in the PCFB, we define the following statistical quantities spatially averaged

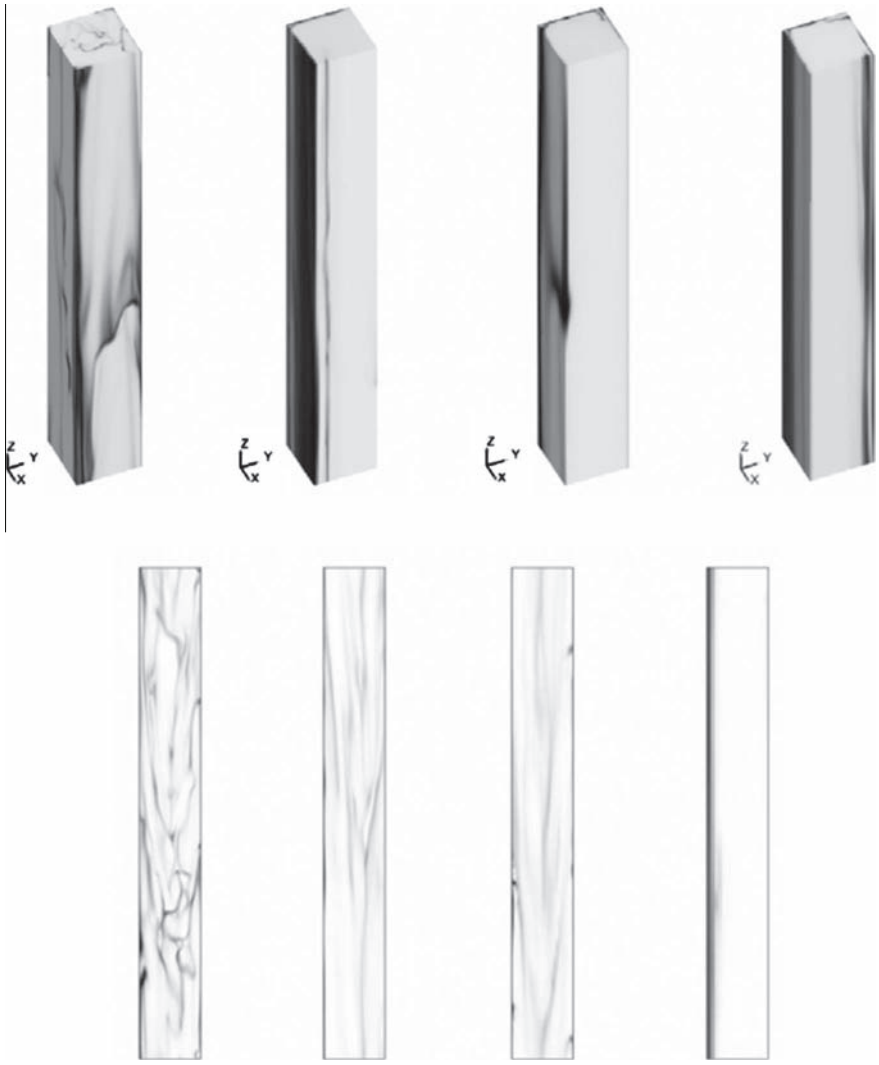

Fig. 2. Instantaneous particle volume fraction field in the periodic circulating fluidized bed for different mesh resolutions (top: 3D view, bottom: *x*–*y* plane). From left to right, the mesh resolution is decreased. White level corresponds to $\alpha_p = 0$, and back level to $\alpha_{p,max} = 0.64$.

Table 1
Simulation parameters and dimensionless numbers for different fluidized bed configurations.

Flow Configuration	A-type (Ref. Case)	A-type (Case-2)	A-type (Case-3)	A/B-type (Case-4)
Bed length, L (m)	0.0275	0.0275	0.11	0.85
Bed height, H (m)	0.22	0.22	0.88	6.79
Initial solid vol. frac., α_{ini}	0.05	0.05	0.05	0.05
Particle diameter, d_p (μm)	75	75	75	125
Particle density, ρ_p (kg/m^3)	1500	3000	3000	3000
Restitution coefficient, e_c	0.9	0.9	0.9	0.9
Gas density, ρ_g (kg/m^3)	1.186	1.186	1.186	1.186
Gas viscosity, μ_g (Pa s)	1.8×10^{-5}	1.8×10^{-5}	1.8×10^{-5}	1.8×10^{-5}
Fr^{-1}	0.106	0.053	0.053	0.024
Ar	22.7	45.4	45.4	210.4
ρ_p/ρ_g	1264.7	2529.5	2529.2	2529.5
L/d_p	366.6	366.6	1466.6	6790
Characteristic velocity, $\tau_p^{St}\lvert\mathbf{g}\rvert$ (m/s)	0.255	0.510	0.510	1.416
Ratio of characteristic length scale to bed height, $\left(\tau_p^{St}\right)^2\lvert\mathbf{g}\rvert/H$	0.03	0.12	0.03	0.03

over the whole domain of volume $\mathcal{V}$ and over a time period T. A time-averaged value $\overline{\langle Q\rangle}^t$ of a spatial-averaged quantity $\langle Q\rangle$ is defined as

$$\overline{\langle Q\rangle}^t = \frac{1}{T}\frac{1}{\mathcal{V}}\int_T\int_{\mathcal{V}} Q(\mathbf{x},t)d\mathbf{x}dt \tag{3}$$

A discrete ensemble averaged value $\overline{\langle Q\rangle}^{t,n}$ over n time instants of the spatial averaged quantity $\langle Q\rangle$ is given by $\overline{\langle Q\rangle}^{t,n} = \sum_{k=1}^{k=n}\langle Q\rangle/n$. The time-spatial averaged relative velocity weighted by solid volume fraction along the mean flow direction is given by $\overline{\langle\alpha_p(U_{p,z}-U_{g,z})\rangle}^t$. The time-spatial averaged solid mass flux along the mean flow direction is calculated by dividing it into two parts: downward and upward. It is calculated by $\overline{\langle G_s\rangle}^t = \overline{\langle G_{s,+}\rangle}^t + \overline{\langle G_{s,-}\rangle}^t$ with downward and upward parts

$$\overline{\langle G_{s,+}\rangle}^t = \overline{\langle\alpha_p\rho_p U_{p,z}\rangle}^t \quad \text{if } U_{p,z} > 0 \tag{4}$$

$$\overline{\langle G_{s,-}\rangle}^t = \overline{\langle\alpha_p\rho_p U_{p,z}\rangle}^t \quad \text{if } U_{p,z} < 0 \tag{5}$$

respectively. For the sake of simplicity, we refer to the time-average of any spatial-average quantity as the average value of the quantity in the following sections. Each simulation was carried out for a long duration to ensure that a statistically stationary state was reached (225 dimensionless physical times with the reference time scale set to the Stokes relaxation time τ_p^{St}). To obtain statistical quantities for all mesh resolutions, an equivalent number of realisations can be ensured by a number of samples calculated by multiplying the number of cells by the dimensionless physical time. For the highest mesh resolution, we carried out the simulation for 225 dimensionless physical times to reach a statistically stationary state and then, we calculated time-averaged value of a quantity over additional 225 dimensionless physical times. The total physical time for the coarsest mesh simulation was 200 times the highest mesh resolution duration.

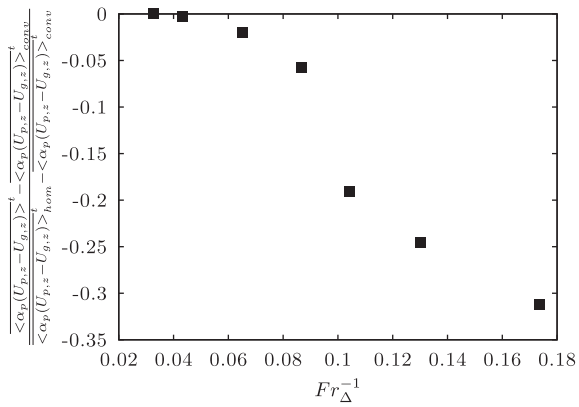

Fig. 3. Influence of mesh size on the weighted gas–particle relative velocity $\overline{\langle\alpha_p(U_{p,z}-U_{g,z})\rangle}^t$. In the vertical axis, *hom* corresponds to the homogeneous case and *conv* corresponds to the converged case, $Fr_\Delta^{-1} = 0.032$.

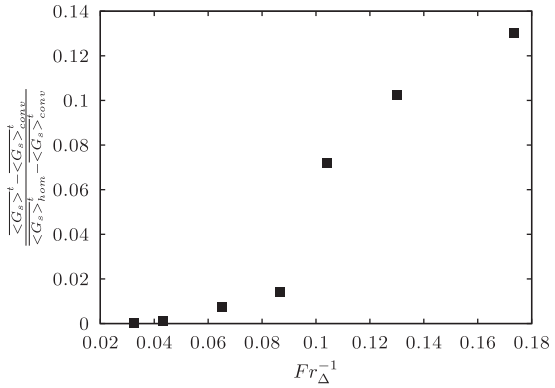

Fig. 4. Influence of mesh size on the total volumetric mass flux $\overline{\langle G_s\rangle}^t$. In the vertical axis, *hom* corresponds to the homogeneous case and *conv* corresponds to the converged case, $Fr_\Delta^{-1} = 0.032$.

After the flow had reached a statistically stationary state, the averaged quantities were gathered. The mesh dependencies of $\overline{\langle\alpha_p(U_{p,z}-U_{g,z})\rangle}^t$ and total vertical solid mass flux (with definitions of *hom*: homogeneous case and *conv*: converged case) are shown by Figs. 3 and 4. The homogeneous case is described by the falling of solids with a homogeneous distribution and the settling velocity $\tau_p^{St}\lvert\mathbf{g}\rvert$. As mesh resolution or Fr_Δ number increases, inhomogeneous structures are better predicted and it can be seen from Fig. 4 that the influence of these structures on the averaged quantities are crucial for solid hold-up in the bed. For the cases where the Fr_Δ number order is 10, the relative velocity and solid mass flux change slightly and converge to constant values. It can be seen from Fig. 5, that the average particle agitation also becomes independent of mesh resolution. The radial distributions of time-averaged variables are shown by Figs. 6–10 for three mesh resolutions: moderate ($32 \times 32 \times 256$, $\Delta_x = \Delta_y = \Delta_z = 8.5 \times 10^{-4}$ m, $Fr_\Delta^{-1} = 0.128$), fine ($64 \times 64 \times 512$, $\Delta_x = \Delta_y = \Delta_z = 4.25 \times 10^{-4}$ m, $Fr_\Delta^{-1} = 0.064$) and finest ($128 \times 128 \times 1024$, $\Delta_x = \Delta_y = \Delta_z = 2.125 \times 10^{-4}$ m, $Fr_\Delta^{-1} = 0.032$). Fig. 6 shows the time-averaged solid volume fraction for different resolutions. The case with moderate resolution predicts a symmetric distribution of solid fraction and accumulation of particles close to the wall. When the mesh resolution is increased, more particles are transported to the centre of the riser than in the moderate case.

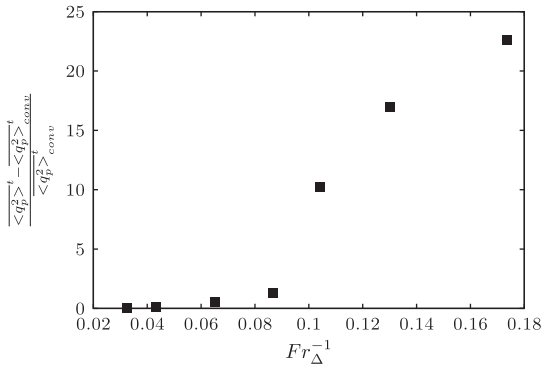

Fig. 5. Influence of mesh size on the particle agitation $\overline{\langle q_p^2 \rangle}^t$. In the vertical axis, *hom* corresponds to the homogeneous case and *conv* corresponds to the converged case, $Fr_\Delta^{-1} = 0.032$.

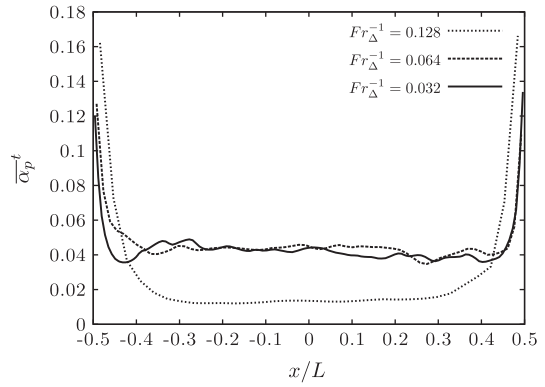

Fig. 6. Radial profile of time-averaged solid volume fraction for three mesh resolutions: moderate ($32 \times 32 \times 256$, $Fr_\Delta^{-1} = 0.128$), fine ($64 \times 64 \times 512$, $Fr_\Delta^{-1} = 0.064$) and finest ($128 \times 128 \times 1024$, $Fr_\Delta^{-1} = 0.032$) (z = 0.11 m, y = 0).

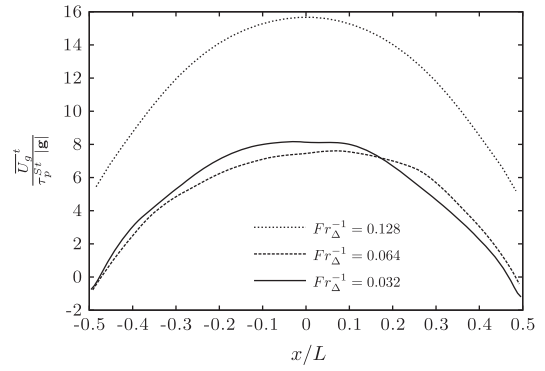

Fig. 7. Radial profile of time-averaged vertical gas velocity for three mesh resolutions: moderate ($32 \times 32 \times 256$, $Fr_\Delta^{-1} = 0.128$), fine ($64 \times 64 \times 512$, $Fr_\Delta^{-1} = 0.064$) and finest ($128 \times 128 \times 1024$, $Fr_\Delta^{-1} = 0.032$) (z = 0.11 m, y = 0).

The time-averaged vertical gas velocities normalised by the settling velocity $\tau_p^{St}|\mathbf{g}|$ are shown by Fig. 7. For moderate mesh resolution, the vertical gas velocity has positive values even close to the wall. With higher mesh resolution, we obtain negative vertical gas velocity close to the wall and a decrease in the mean flow magnitude. Figs. 8 and 9 present negative, positive and total vertical solid mass flux normalised by the uniform distribution of solid falling with settling velocity $\tau_p^{St}|\mathbf{g}|$. The core-annulus flow is obtained for moderate, fine and finest mesh resolutions and they descend only in the vicinity of the wall. The negative vertical solid mass flux decreases close to the wall with increasing mesh resolution due to the better predic-

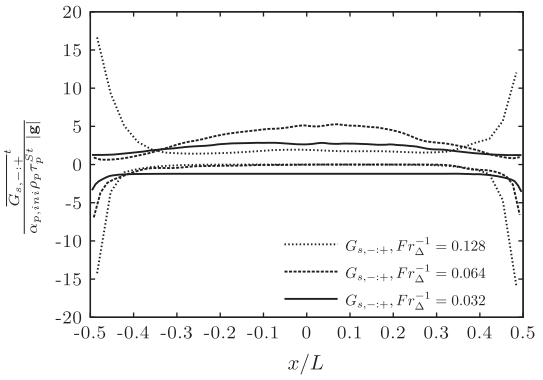

Fig. 8. Radial profile of time-averaged negative and positive vertical solid mass flux for three mesh resolutions: moderate ($32 \times 32 \times 256$, $Fr_\Delta^{-1} = 0.128$), fine ($64 \times 64 \times 512$, $Fr_\Delta^{-1} = 0.064$) and finest ($128 \times 128 \times 1024$, $Fr_\Delta^{-1} = 0.032$) (z = 0.11 m, y = 0).

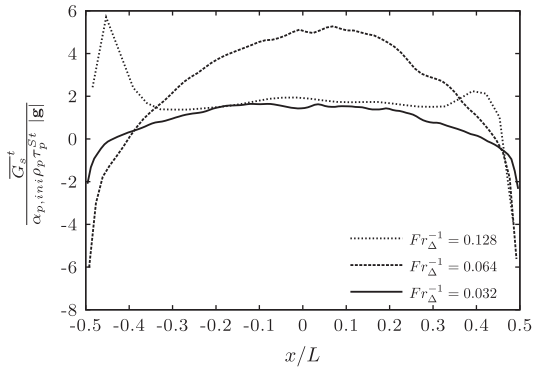

Fig. 9. Radial profile of time-averaged total vertical solid mass flux for three mesh resolutions: moderate ($32 \times 32 \times 256$, $Fr_\Delta^{-1} = 0.128$), fine ($64 \times 64 \times 512$, $Fr_\Delta^{-1} = 0.064$) and finest ($128 \times 128 \times 1024$, $Fr_\Delta^{-1} = 0.032$) (z = 0.11 m, y = 0).

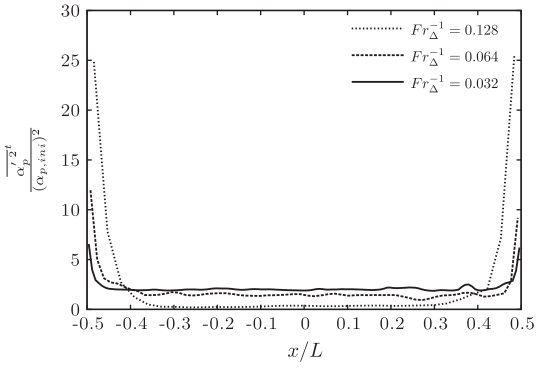

Fig. 10. Radial profile of time-averaged variance of solid volume fraction for three mesh resolutions: moderate ($32 \times 32 \times 256$, $Fr_\Delta^{-1} = 0.128$), fine ($64 \times 64 \times 512$, $Fr_\Delta^{-1} = 0.064$) and finest ($128 \times 128 \times 1024$, $Fr_\Delta^{-1} = 0.032$) (z = 0.11 m, y = 0).

tion of flow mixing. Fig. 10 shows the variance of the solid volume fraction normalised by the initial solid volume fraction. The variance of solid volume fraction, which represents the clustering effect, reaches its maximum value close to the wall. The finest mesh resolution ($128 \times 128 \times 1024$, $Fr_\Delta^{-1} = 0.032$) results are then used to construct a database of solid volume fraction, gas and particle velocities obtained on 10 time instants. These time instants were chosen every 20 Stokes relaxation times τ_p^{St} during the statistically-steady-state period of the simulation. This database is called a Euler–Euler

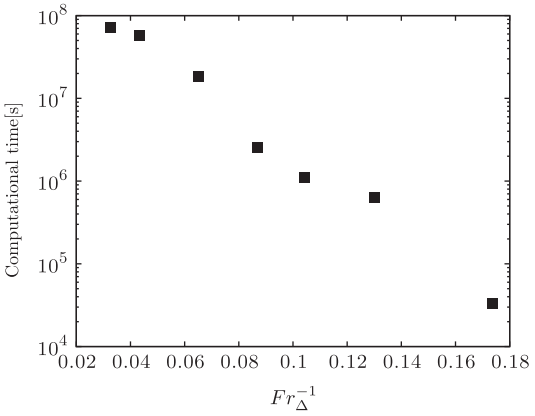

Fig. 11. CPU times required to simulate 1 s of the flow using the kinetic theory based Euler–Euler model for the reference case.

DNS database and consists of 180 million realisations of macroscopic variables. Then, we perform volume averaging on these variables.

Fig. 11 shows the CPU times required to compute 1 s of the flow for the reference case. CPU time increases almost linearly with the mesh resolution. The computational time needed to reach statistically converged results is about 25 days on 512 processors[1] for the case with the finest mesh resolution. Due to computational limits (see the CPU time required for the mesh resolution $Fr_{\Delta}^{-1} = 0.032$), fully resolved simulations using the Euler–Euler model for industrial size fluidised beds are unaffordable. For details of high-performance computing with NEPTUNE_CFD, see Neau et al. (2010).

By following Anderson and Jackson (1967), Anderson and Jackson (1968), the independent dimensionless parameters governing the fluidised bed dynamics are found by dimensional analysis of the differential equations governing the fluid and particulate phases. From a dimensional analysis based on Buckingham's π-theorem, the possible set includes the inverse Froude number $Fr^{-1} = \sqrt{gd_p}/U_g$, solid loading $G_s/\rho_g U_g$, Archimedes number $Ar = \rho_p \rho_g d_p^3 g/\mu_g^2$, the density ratio ρ_p/ρ_g and the ratio of riser diameter to particle diameter L/d_p. U_g represents the superficial gas velocity and G_s is the average solid mass flux. This set of variables can be used to perform the mesh dependency studies of Geldart A and A/B particle inventories in the 3D PCFB. In the present work, we substitute the superficial gas velocity U_g by a single particle terminal velocity $\tau_p^{St}|\mathbf{g}|$. Additionally, the particle diameter is replaced by a mesh size to show the mesh dependency of the solid mass fluxes for different types of particles. The dimensionless parameters of the numerical simulations are summarised in Table 1 and the characteristic mesh sizes for different particle types are given in Table 2. The time- and spatial-averaged solid fluxes with respect to the inverse Froude number Fr_{Δ}^{-1} based on the mesh size are shown by Fig. 12. As expected, the mesh resolution needed for Euler–Euler DNS of type A/B particles is significantly smaller than for type A particles. However, it can be seen that Fr_{Δ}^{-1} is not a universal dimensionless number describing the mesh dependency of different particles and this outcome has to be taken into consideration for the modelling of the effective drag force.

3. Budget analysis of filtered particulate momentum equation

Mesh-independent results obtained in the previous section are now used for budget analyses of the filtered particle momentum and agitation equations. The derivation of filtered Euler–Euler two-phase model is given in Appendix B. Additional terms (Eqs. B.18, (B.19)–(B.22)) arising due to volume filtering require closure models. These budget analyses allow us to examine the contributions of additional terms and to neglect some of them depending on their importance. To obtain better insight into the influences of additional terms in the filtered momentum equation of the particulate phase, filtered and sub-grid contribution terms are calculated for different filter widths $\overline{\Delta}$. The average of the filtered particulate momentum balance along the mean flow reads

$$
\begin{aligned}
0 = &-\overline{\left\langle \bar{\alpha}_p \frac{\partial \widetilde{P}_g}{\partial z} \right\rangle}^{t,n} - \overline{\langle \varphi_{p,z}^{sgs} \rangle}^{t,n} + \overline{\left\langle \frac{\bar{\alpha}_p \rho_p}{\tilde{\tau}_p} \left(\widetilde{U}_{g,z} - \widetilde{U}_{p,z} \right) \right\rangle}^{t,n} \\
&+ \overline{\left\langle I_{p,z}^{sgs} \right\rangle}^{t,n} - \overline{\left\langle \frac{\partial}{\partial x_j} \widetilde{\Sigma}_{p,zj} \right\rangle}^{t,n} - \overline{\left\langle \frac{\partial}{\partial x_j} \Sigma_{p,zj}^{sgs} \right\rangle}^{t,n} \\
&- \overline{\left\langle \frac{\partial}{\partial x_j} \rho_p \bar{\alpha}_p \sigma_{p,zj}^{sgs} \right\rangle}^{t,n} + \overline{\left\langle \bar{\alpha}_p \rho_p g_z \right\rangle}^{t,n}
\end{aligned}
\tag{6}
$$

Eq. (6) states the global equilibrium of fluidised particles considering buoyancy force (gas pressure gradient), drag force, particulate stress and gravity contributions. The first and second terms represent the filtered and sub-grid buoyancy force. The third and fourth terms are the filtered and sub-grid drag force. The second line shows the filtered, sub-grid particulate kinetic stress tensor and the sub-grid contribution of particle phase velocity fluctuations. The last term is the gravity contribution.

The filtered and the sub-grid contributions of each term normalised by the gravity term for inverse Froude numbers Fr_{Δ}^{-1} based on the filter width $\overline{\Delta}$ are shown by Figs. 13 and 14. It can be seen that drag and gravity forces are the main contributions of the filtered momentum equation. This result is consistent with the findings of Zimmermann and Taghipour (2005). The sub-grid contribution of the drag force increases dramatically as filter width increases. The filtered drag force increases with the similar behaviour and the sum of filtered and sub-grid contribution of drag force remains constant (see Fig. 13). The drag term is overestimated if the sub-grid contribution is not taken into account. This outcome is in agreement with those of Agrawal et al. (2001) and Parmentier et al. (2012). The order of the sub-grid contribution of buoyancy force without the hydrostatic part (mean vertical gas pressure drop

Table 2
Mesh resolutions of different fluidized bed configurations.

	Fr_{Δ}^{-1}						
Ref. Case	0.1722	0.1291	0.1033	0.0861	0.0645	0.0430	0.0322
Case-2	0.0430	0.0322	0.0258	0.0215	0.0161	0.0107	
Case-3	0.1722	0.1291	0.1033	0.0861	0.0645	0.0430	
Case-4	0.1722	0.1291	0.1033	0.0861			

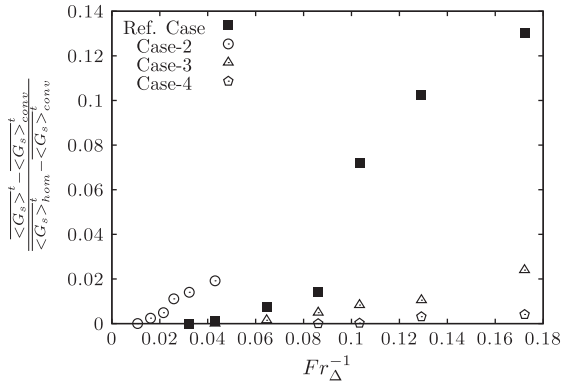

Fig. 12. Influence of mesh size on the total vertical solid mass flux $\overline{\langle G_s \rangle}^t$ for different type of Geldart particles (for details, see Table 1). In the vertical axis, *hom* corresponds to the homogeneous case and *conv* corresponds to the converged case.

[1] The simulations were performed on Bi-Xeon E5472 processors running at 3 GHz.

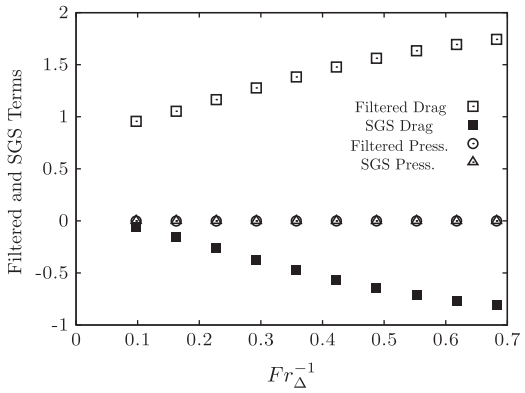

Fig. 13. Filtered and sub-grid contributions drag force and gas pressure gradient without hydrostatic part normalised by the gravity term for different inverse Froude numbers Fr_{Δ}^{-1} based on the filter width $\overline{\Delta}$.

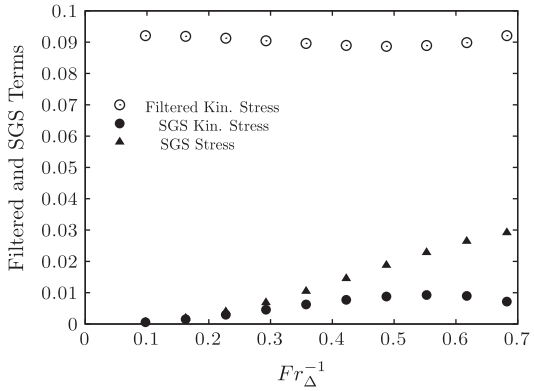

Fig. 14. Filtered and sub-grid contributions of particulate and sub-grid stress terms normalised by the gravity term for different inverse Froude numbers Fr_{Δ}^{-1} based on the filter width $\overline{\Delta}$.

set to balance of total mass on the riser) is the same as that of the filtered buoyancy for intermediate and large filter widths. The filtered particulate stress contribution is independent of filter width and the sub-grid contribution can be negligible (see Fig. 14). The sub-grid stress tensor contribution increases asymptotically as filter width increases and it is expected to reach the value of the filtered particulate stress contribution for large filter widths. Zhang and VanderHeyden (2002) and De Wilde (2005) state that the buoyancy term has to be taken into account for simulations with coarse meshes. However, we observe that the sub-grid contribution of the drag force is much greater than that of the buoyancy term. Several studies have been devoted to the influence of meso-scale structures on the sub-grid stress tensor. Dasgupta et al. (1994) solved unsteady fully developed flow in a vertical riser with a Reynolds averaging equation model based on the mixing velocity in the framework of turbulence modelling. The additional transport equations of the turbulent kinetic energy k and the turbulent rate of dissipation ϵ were coupled with mixture mass and momentum balances. They revealed that particles were driven to regions having a low intensity of particle-phase velocity fluctuations from regions of high intensity at rates proportional to the gradients in the intensity of fluctuations. Hrenya and Sinclair (1997) applied Reynolds decomposition to the gas and particulate equations separately and described the Reynolds stresses for the particulate phase with a turbulent viscosity assumption. It was found that the turbulent viscosity of the particulate phase significantly flattened mean variable profiles. Considering the consequences of previous studies with our analyses, here, we pay attention to drag and particle sub-grid stress tensor terms to investigate their influence on the clustering effect.

3.1. Analyses of sub-grid and filtered contributions in drag term

We state that, if the sub-grid contribution of the drag force is not taken into account, the resolved drag force may be over-predicted, leading to poor prediction of the overall fluidised bed behaviour. The filtered drag force is written as

$$\overline{\frac{\alpha_p\rho_p}{\tau_p}V_{r,i}} = \frac{\bar{\alpha}_p\rho_p}{\tilde{\tau}_p}\left(\widetilde{U}_{g,i} - \widetilde{U}_{p,i}\right) + I_{p,i}^{sgs} \tag{7}$$

where $I_{p,i}^{sgs}$ is the sub-grid contribution of the drag force. By following Ozel et al. (2010) and Parmentier et al. (2012), the filtered drag force can be approximated by the following expression:

$$\overline{\frac{\alpha_p\rho_p}{\tau_p}V_{r,i}} \simeq \frac{\rho_p}{\tilde{\tau}_p}\overline{\alpha_p V_{r,i}} \tag{8}$$

with the filtered relaxation time $\tilde{\tau}_p$ given by

$$\tilde{\tau}_p = \frac{4}{3}\frac{\rho_p}{\rho_g}\frac{d_p}{C_D^*|\widetilde{\mathbf{V}}_r|} \tag{9}$$

The filtered drag coefficient C_D^* is

$$C_D^* = \frac{24}{Re_p^*}\left[1 + 0.15\left(Re_p^*\right)^{0.687}\right]\bar{\alpha}_g^{-1.7} \tag{10}$$

with the filtered particle Reynolds number Re_p^* given by $\frac{d_p|\widetilde{\mathbf{V}}_r|}{\nu_g}$. The correlation coefficients[2] between the left- and right-hand sides of Eq. (8) are around 99% for each direction, even for a large filter width. We propose to write the mean relative velocity as

$$\overline{\alpha_p V_{r,i}} = \bar{\alpha}_p(\widetilde{U}_{p,i} - \widetilde{U}_{g,i} - \widetilde{V}_{d,i}) \tag{12}$$

by introducing the sub-grid drift velocity $\widetilde{V}_{d,i}$. Thus, the sub-grid drift velocity is defined by

$$\bar{\alpha}_p\widetilde{V}_{d,i} = \overline{\alpha_p U_{g,i}} - \bar{\alpha}_p\widetilde{U}_{g,i} \tag{13}$$

and the sub-grid contribution of the drag force may be modelled as

$$I_{p,i}^{sgs} \simeq \frac{\bar{\alpha}_p\rho_p}{\tilde{\tau}_p}\widetilde{V}_{d,i} \tag{14}$$

The sub-grid drag force contribution is then directly proportional to the sub-grid drift velocity which is, by definition, the difference between the filtered gas velocity weighted by the particle volume fraction and the filtered gas velocity weighted by the gas volume fraction. This definition is consistent with the study by Zhang and VanderHeyden (2002). The sub-grid drift velocity physically accounts for the correlation between inhomogeneities of solid volume fraction and gas velocity inside the volume filtering. The sub-grid drift velocity $\widetilde{V}_{d,i}$ cannot be directly obtained from the kinetic-theory-based numerical simulation and needs a specific closure.

3.2. Analyses of particle sub-grid scale stress tensor contribution

The particle SGS stress tensor is defined in Eq. (B.4) as

$$\sigma_{p,ij}^{sgs} = \widetilde{U_{p,i}U_{p,j}} - \widetilde{U}_{p,i}\widetilde{U}_{p,j} \tag{15}$$

In incompressible single-phase flow, the trace of the sub-grid stress tensor is not modelled but is incorporated into the filtered pressure. In the context of dispersed phase, the trace of $\sigma_{p,ij}^{sgs}$ has

[2] Pearson correlation coefficients between fields A and B are given by

$$r(A;B) = \frac{\langle AB\rangle - \langle A\rangle\langle B\rangle}{\sqrt{(\langle A^2\rangle - \langle A\rangle^2)(\langle B^2\rangle - \langle B\rangle^2)}} \tag{11}$$

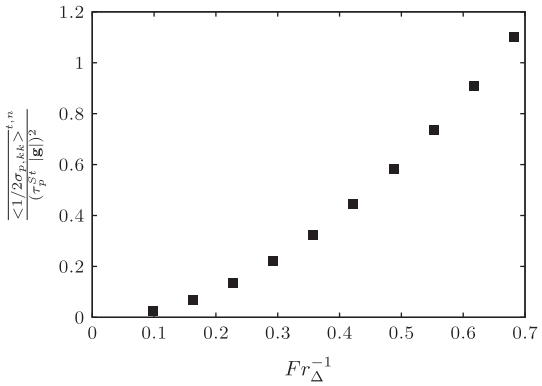

Fig. 15. Averaged sub-grid correlated energy $1/2\sigma_{p,kk}$ for different inverse Froude numbers Fr_Δ^{-1} based on the filter width $\overline{\Delta}$.

the dispersive characteristic and it is crucial to the obtention of a better prediction of particle segregation (Moreau et al., 2009). Then, the particle sub-grid stress tensor $\sigma_{p,ij}^{sgs}$ is divided into deviatoric and spherical parts:

$$\sigma_{p,ij}^{sgs} = \sigma_{p,ij}^{*} + \frac{1}{3}\sigma_{p,kk}\delta_{ij} \tag{16}$$

The sub-grid correlated energy is given by $1/2\sigma_{p,kk}$ and shown for inverse Froude numbers Fr_Δ^{-1} based on the filter width $\overline{\Delta}$ (Fig. 15). As expected, the sub-grid correlated energy increases almost linearly with the filter width (as in single-phase turbulent flows). Fig. 16 compares the sub-grid correlated energy and the filtered particulate stress tensor trace $\left(\widetilde{P}_p - \tilde{\lambda}_p \frac{\partial \widetilde{U}_{p,m}}{\partial x_m}\right)$. Both terms are conditionally averaged by filtered solid volume fraction. It is revealed that the sub-grid correlated energy is larger than the filtered particulate stress tensor trace, especially for larger filter widths. The deviatoric part of the particle sub-grid stress tensor can be studied at the scalar level (dissipation) by multiplying the tensor by the particle velocity gradients. The sub-grid dissipations by the correlated and filtered particulate stress tensors are given by respectively $\sigma_{p,ij}^{*}\frac{\partial \widetilde{U}_{p,i}}{\partial x_j}$ and $\tilde{\nu}_p \widetilde{S}_{p,ij}^{*}\frac{\partial \widetilde{U}_{p,i}}{\partial x_j}$ where $\widetilde{S}_{p,ij}^{*} = \frac{\partial \widetilde{U}_{p,i}}{\partial x_j} + \frac{\partial \widetilde{U}_{p,j}}{\partial x_i} - \frac{2}{3}\frac{\partial \widetilde{U}_{p,m}}{\partial x_m}\delta_{ij}$ is the trace-free strain-rate tensor. The conditional averages of these terms by filtered volume fraction are shown by Fig. 17. It is clear that sub-grid dissipation is larger than the filtered particulate stress dissipation. It can be concluded that the sub-grid correlated energy $1/2\sigma_{p,kk}$ and dissipation

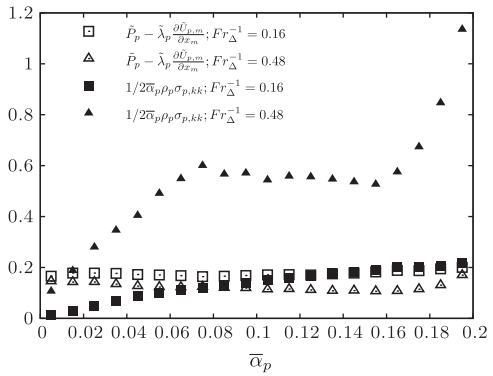

Fig. 16. Filtered particulate stress tensor trace $\widetilde{P}_p - \tilde{\lambda}_p \frac{\partial \widetilde{U}_{p,m}}{\partial x_m}$ and sub-grid correlated energy $1/2\overline{\alpha}_p\rho_p\sigma_{p,kk}$ conditionally averaged by filtered volume fraction for inverse Froude numbers $Fr_\Delta^{-1} = 0.16$ and $Fr_\Delta^{-1} = 0.48$ based on the filter width $\overline{\Delta}$ (normalised $\langle\overline{\alpha}_p\rangle\rho_p\left(\tau_p^{St}|\mathbf{g}|\right)$).

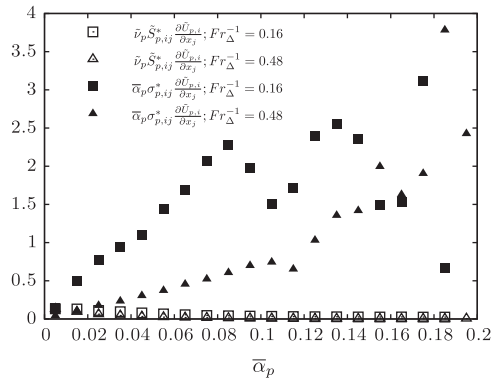

Fig. 17. Filtered particulate stress dissipation $\tilde{\nu}_p\widetilde{S}_{p,ij}^{*}\frac{\partial \widetilde{U}_{p,i}}{\partial x_j}$ and sub-grid dissipation $\tilde{\alpha}_p\sigma_{p,ij}^{*}\frac{\partial \widetilde{U}_{p,i}}{\partial x_j}$ conditionally averaged by filtered volume fraction for inverse Froude numbers $Fr_\Delta^{-1} = 0.16$ and $Fr_\Delta^{-1} = 0.48$ based on the filter width $\overline{\Delta}$ (normalised $\langle\overline{\alpha}_p\rangle\rho_p\left(\tau_p^{St}|\mathbf{g}|\right)^2$).

due to sub-grid stress $\sigma_{p,ij}^{*}\frac{\partial \widetilde{U}_{p,i}}{\partial x_j}$ has to be taken into account for simulations with mesh sizes larger than the small-scale structure, and sub-grid contributions of kinetic-theory-based stresses can be ignored.

4. Budget analysis of filtered transport equation of particle agitation

By following the budget analysis of the filtered particulate momentum equation, the contributions of additional terms in the filtered transport equation of particle agitation are calculated for different filter widths. The particle agitation balance is defined as follows:

$$\begin{aligned} 0 = &\overline{\left\langle \frac{\partial}{\partial x_i}\left(\bar{\alpha}_p\rho_p\left(\widetilde{K}_p^{kin} + \widetilde{K}_p^{coll}\right)\frac{\partial \tilde{q}_p^2}{\partial x_i}\right)\right\rangle^{t,n}} + \overline{\left\langle \frac{\partial}{\partial x_i}\left(\rho_p\mathcal{K}_i\right)\right\rangle^{t,n}} \\ &- \overline{\left\langle \widetilde{\Sigma}_{p,ij}\frac{\partial \widetilde{U}_{p,j}}{\partial x_i}\right\rangle^{t,n}} - \overline{\langle\mathcal{V}\rangle}^{t,n} - \overline{\left\langle \frac{1}{3}\left(1-e_c^2\right)\frac{\bar{\alpha}_p\rho_p}{\tilde{\tau}_c}\tilde{q}_p^2\right\rangle^{t,n}} \\ &- \overline{\langle\mathcal{E}\rangle}^{t,n} - \overline{\left\langle 2\frac{\bar{\alpha}_p\rho_p}{\tilde{\tau}_p}\tilde{q}_p^2\right\rangle^{t,n}} - \overline{\langle\mathcal{S}\rangle}^{t,n} - \overline{\langle\mathcal{Q}\rangle}^{t,n} \end{aligned} \tag{17}$$

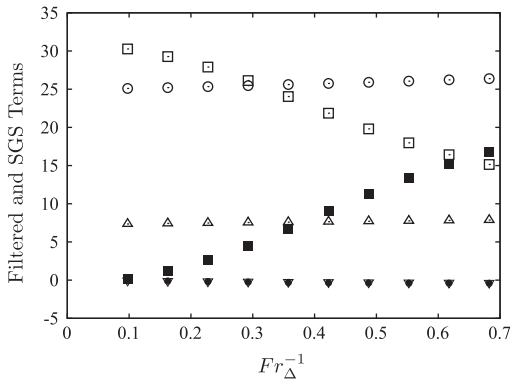

Fig. 18. Filtered and sub-grid contributions of production and destruction of the particle agitation, as given in Eq. (17), normalised by $\rho_p\left(\tau_p^{St}\right)^2|\mathbf{g}|^2$ for different inverse Froude numbers Fr_Δ^{-1} based on the filter width $\overline{\Delta}$. Production; □: filtered and ■: sub-grid, Destruction; △: filtered and ▽: sub-grid, Interaction with fluid; ○: filtered and •: sub-grid (symbols ▽ and • are overlapping and close to zero).

Eq. (17) states the global equilibrium of particle agitation between transport by velocity fluctuations, production mechanism, destruction by inelastic collisions, and interaction with the gas. The first and second terms represent the filtered and the sub-grid kinetic and collisional diffusivity. The third and fourth terms are the filtered and the sub-grid contribution of the production of agitation by the filtered particle velocity gradients. The loss of energy due to collisions on the filtered and the sub-grid terms are accounted for by the fifth and the sixth terms. The seventh and eighth terms represent the filtered and sub-grid interaction of agitation with gas phase. The last term is the sub-grid particle agitation flux.

Fig. 18 shows that the sub-grid contributions of destruction by interaction with the fluid and the sub-grid contribution of dissipation can be negligible. In contrast, the sub-grid contribution of production is significant. For coarse grid simulation, these terms are not taken into account and this leads to underestimation of the production of particle agitation. The rates of production are smaller for coarse grid simulations due to diminished clustering non-uniformity and smaller magnitudes of velocity gradients. Agrawal et al. (2001) determined domain-averaged values of the production term and the same consequences were obtained for dilute gas–solid flow. The sub-grid contribution of diffusivity of particle agitation and the SGS particle agitation flux can be neglected (see Fig. 19).

5. Modelling of effective drag force

The analogy can be constructed between SGS scalar flux in single-phase turbulent flows and the sub-grid drift velocity defined by Eq. (13). The modelling of the SGS scalar flux in single-phase turbulent flows is presented briefly below and the capabilities for modelling the sub-grid contribution of the drag force are investigated. The sub-grid drift velocity can be modelled by a Smagorinsky-type model, as also referred to as the functional model, and structural models such as the Gradient and the Scale Similarity models (Sagaut, 2004). The Smagorinsky model is based on the eddy viscosity concept and accounts for the sub-grid scale scalar flux in terms of the resolved strain-rate tensor and the scalar gradients. The Gradient model assumes that the SGS scalar flux can be modelled as a function of a tensor which is the product of the filtered scalar gradient and the filtered velocity gradient Clark et al. (1979), as follows:

$$\theta_i = C_{gr}\overline{\Delta}^2 \frac{\partial \overline{\xi}}{\partial x_j}\frac{\partial \widetilde{U}_i}{\partial x_j} \tag{18}$$

where $\overline{\Delta}$ is the filter width, C_{gr} is the model constant to be determined by comparison with the DNS database, θ_i is the SGS scalar flux, $\widetilde{U}_j$ is the j component of the Favre averaged flow velocity and $\overline{\xi}$ is the averaged scalar.

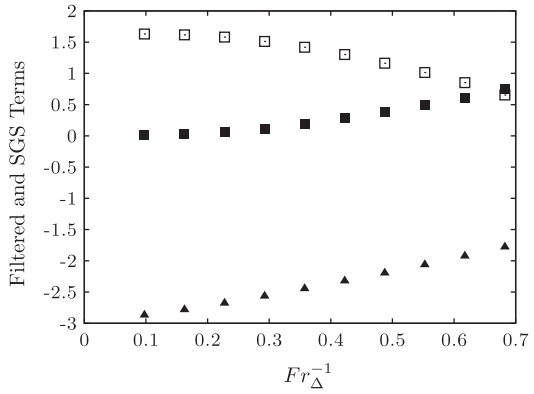

Fig. 19. Filtered and sub-grid contributions of particle diffusivity term and sub-grid particle agitation flux, as given in Eq. (17), normalised by $\rho_p\left(\tau_p^{St}\right)^3|\mathbf{g}|^2$ for different inverse Froude numbers Fr_{Δ}^{-1} based on the filter width $\overline{\Delta}$. Kinetic diffusivity; □: resolved ■: sub-grid, ▲: Sub-grid particle agitation flux.

The Scale Similarity model assumes that the full structure of the velocity field below $\overline{\Delta}$ is similar to that at scales above $\overline{\Delta}$ (Bardina et al., 1983). This model introduces a second filter having a given scale $\gamma\overline{\Delta}$, with $\gamma \geqslant 1$. The SGS scalar flux is modelled as proportional to the difference between the re-filtered product of filtered velocity and the scalar, and the product of the re-filtering of the filtered velocity and the scalar:

$$\theta_i = C_{ss}\left(\widehat{\overline{\xi}\widetilde{U}_i} - \widehat{\overline{\xi}}\,\widehat{\widetilde{U}}_i\right) \tag{19}$$

where $\wedge$ is the second filter and C_{ss} is a given constant. The original model was proposed by Bardina et al. (1983) and γ was set to 1. Various versions of this model have been proposed, such as that by Liu et al. (1994) in which γ was set to 2. The Gradient and the Scale Similarity models can be directly applied to model the sub-grid drift velocity where the solid volume fraction is introduced as a scalar. However, the interactions between resolved and unresolved scales have not been well-established, in contrary to the Smagorinsky model for single-phase turbulent flows. Intensive correlation analyses between the sub-grid drift velocity and filtered variables have to be performed to prescribe the sub-grid contribution of drag in terms of filtered quantities for the Smagorinsky-type sub-grid model. The sub-grid drift velocity models will be evaluated here with *a priori* tests. The mesh-independent results, which have sufficient spatial resolution to allow the determination of sub-grid quantities, are filtered, the models are applied to the filtered data and then the model estimates are compared with actual values determined directly from the filtered mesh-independent results. Volume averaging, as described in Appendix B, is used for the filtering process.

The primary interest is the accuracy of the sub-grid drift velocity models, which can be assessed by computing a correlation coefficient between model predictions and exact values calculated from mesh-independent results. The correlation coefficient r, computed as in Eq. (11), shows the *a priori* predictability of basic model assumptions by quantifying the degree to which the structure of $\bar{\alpha}_p\widetilde{V}_{d,i}$ is captured by the models. Meanwhile, to quantify the statistical accuracy of the models, we define the relative error as

$$e \equiv \frac{\text{model-measured}}{\langle(\text{measured})^2\rangle^{1/2}} \tag{20}$$

and the mean squared error as

$$E \equiv \frac{\langle(\text{model-measured})^2\rangle^{1/2}}{\langle(\text{measured})^2\rangle^{1/2}} \tag{21}$$

5.1. Functional model

Correlation coefficients were calculated between $\bar{\alpha}_p\widetilde{V}_{d,i}$ and filtered variables for different inverse Froude numbers Fr_{Δ}^{-1} based on the filter width $\overline{\Delta}$ along the mean flow direction. They are shown by Fig. 20. $\bar{\alpha}_p\widetilde{V}_{d,z}$ is strongly related to $\bar{\alpha}_p(\widetilde{U}_{g,z} - \widetilde{U}_{p,z})$ for larger filter widths. We have a more uniform flow structure and the gas velocity and particle volume fraction are not strongly correlated for larger filter widths. The dependency of $\bar{\alpha}_p\widetilde{V}_{d,z}$ on the variable $\bar{\alpha}_p(\widetilde{U}_{g,z} - \widetilde{U}_{p,z})$ for different inverse Froude numbers Fr_{Δ}^{-1} can be seen on the scatter plots (see Fig. 21).

Because of the difficulty of displaying plots of all the data, $\bar{\alpha}_p\widetilde{V}_{d,z}$ and $\bar{\alpha}_p(\widetilde{U}_{g,z} - \widetilde{U}_{p,z})$ were randomly sampled. Based on the correlation analysis on the sub-grid drag term, we propose to model $\bar{\alpha}_p\widetilde{V}_{d,i}$ (see Ozel et al., 2010; Parmentier et al., 2012) as

$$\bar{\alpha}_p\widetilde{V}_{d,i} = g_{ij}(\Delta^*, \bar{\alpha}_p)\bar{\alpha}_p\left(\widetilde{U}_{g,j} - \widetilde{U}_{p,j}\right) \tag{22}$$

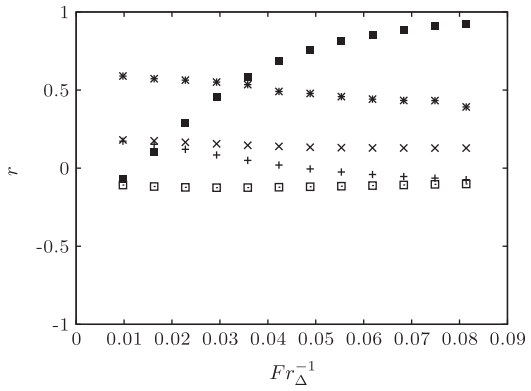

Fig. 20. Correlation coefficients between $I_{p,z}^{sgs}/\frac{\rho_p}{\tau_p}$ and filtered variables for different inverse Froude numbers Fr_{Δ}^{-1} based on the filter width $\overline{\Delta}$: $+$: $\bar{\alpha}_p\tau_p^{St}|\mathbf{g}|$, $\times$: $\left(\tau_p^{St}\right)^3|\mathbf{g}|^2\frac{\partial\bar{\alpha}_p}{\partial z}$, $*$: $\left(\tau_p^{St}\right)^4|\mathbf{g}|^2||\nabla\bar{\alpha}_p||\frac{\partial\widetilde{U}_{g,z}}{\partial z}$, $\boxdot$: $\left(\tau_p^{St}\right)^4|\mathbf{g}|^2\frac{\partial\bar{\alpha}_p}{\partial z}\frac{\partial\widetilde{U}_{p,z}}{\partial z}$, $\blacksquare$: $\bar{\alpha}_p(\widetilde{U}_{p,z}-\widetilde{U}_{g,z})$.

where g_{ij}, the drag correction tensor, is a function of the dimensionless length scale Δ^* and the filtered particle volume fraction $\bar{\alpha}_p$. We assume that g_{ij} is diagonal ($g_{ij}=0$ if $i\neq j$) and $g_{xx}=g_{yy}=\lambda$ g_{zz} in the specific frame where the mean flow direction ($z-$) is aligned with the direction of gravity acceleration. The function $g(\Delta^*,\bar{\alpha}_p)$ can be calculated from the mesh-independent results for a given flow configuration with different filter widths by the following relation:

$$g(\Delta^*,\bar{\alpha}_p)\frac{\overline{\langle\bar{\alpha}_p\widetilde{V}_{d,z}|\bar{\alpha}_p\rangle^{t,n}}}{\left\langle\left[\bar{\alpha}_p(\widetilde{U}_{g,z}-\widetilde{U}_{p,z})\right]\middle|\bar{\alpha}_p\right\rangle^{t,n}} \tag{23}$$

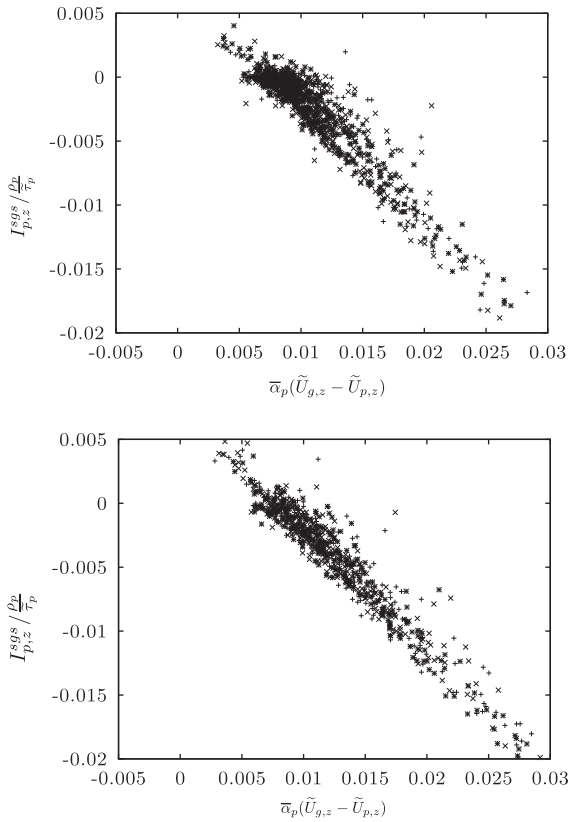

Fig. 21. Scattering plot of $I_{p,z}^{sgs}/\frac{\rho_p}{\tau_p}$ with respect to $\bar{\alpha}_p(\widetilde{U}_{g,z}-\widetilde{U}_{p,z})$ for intermediate and large inverse Froude numbers Fr_{Δ}^{-1} based on the filter width $\overline{\Delta}$: $*$: $Fr_{\Delta}^{-1}=0.224$, $\times$: $Fr_{\Delta}^{-1}=0.288$, $+$: $Fr_{\Delta}^{-1}=0.416$ (top) and $*$: $Fr_{\Delta}^{-1}=0.544$, $\times$: $Fr_{\Delta}^{-1}=0.618$, $+$: $Fr_{\Delta}^{-1}=0.683$ (bottom).

$\bar{\alpha}_p\widetilde{V}_{d,z}$ and $\bar{\alpha}_p(\widetilde{U}_{g,z}-\widetilde{U}_{p,z})$ are conditionally averaged by the filtered solid volume fraction. In a general form, the proposed model can be written

$$\bar{\alpha}_p\widetilde{V}_{d,\beta}=K_{\beta\beta}g(\Delta^*,\bar{\alpha}_p)\bar{\alpha}_p\left(\widetilde{U}_{g,\beta}-\widetilde{U}_{p,\beta}\right) \tag{24}$$

where $\beta=x,y,z$ and β is used to indicate that there is no implicit summation. The model constant $K_{\beta\beta}$ is case-dependent and dynamically adjusted by following the methodology of Germano et al. (1991), Lilly (1992) and Parmentier et al. (2012). Then, the effective drag term can be written as

$$\overline{\frac{\alpha_p\rho_p}{\tau_p}V_{r,\beta}}=\frac{\rho_p}{\overline{\tau}_p}\left[1+K_{\beta\beta}g(\Delta^*,\bar{\alpha}_p)\right]\bar{\alpha}_p\left(\widetilde{U}_{g,\beta}-\widetilde{U}_{p,\beta}\right) \tag{25}$$

This definition is consistent with the studies by Zhang and VanderHeyden (2002), Heynderickx et al. (2004), Andrews et al. (2005), and Igci et al. (2008). An effective drag coefficient β_e was introduced by these authors to express the filtered drag force term as

$$\overline{\frac{\alpha_p\rho_p}{\tau_p}V_{r,i}}=\beta_e\left(\widetilde{U}_{g,i}-\widetilde{U}_{p,i}\right) \tag{26}$$

Heynderickx et al. (2004) and Andrews et al. (2005) write the effective drag coefficient as a function of the filtered particle volume fraction, while Igci et al. (2008) suggest that this coefficient is a function of the filter width. Igci and Sundaresan (2011) proposed an extended model with a function of both the filtered volume fraction and the filter width. McKeen and Pugsley (2003), Hosseini et al. (2009) and Gao et al. (2008) suggested using a constant scale factor for the effective drag coefficient. However, the predictability of this model based on a constant scale factor is case limited.

The function $g(\Delta^*,\bar{\alpha}_p)$ for different inverse Froude numbers Fr_{Δ}^{-1} based on the filter width $\overline{\Delta}$ along the mean flow direction are shown by Fig. 22. The normalised function

$$\frac{g(\Delta^*,\bar{\alpha}_p)}{\int g(\Delta^*,\bar{\alpha}_p)d\bar{\alpha}_p} \tag{27}$$

is nearly independent of Δ^* (see Fig. 23). Then, introducing the function $f(\Delta^*)=\int g(\Delta^*,\bar{\alpha}_p)d\bar{\alpha}_p$, we decompose $g(\Delta^*,\bar{\alpha}_p)$ as

$$g(\Delta^*,\bar{\alpha}_p)\approx f(\Delta^*)h(\bar{\alpha}_p) \tag{28}$$

The function $h(\bar{\alpha}_p)$ accounts for the volume fraction dependence of the model. The function $f(\Delta^*)$, which represents the filter dependence of the model, will be constructed in detail later. The function $h(\bar{\alpha}_p)$ is nearly equal to zero for values of $\bar{\alpha}_p$ greater than 0.62 and this means that the correction for drag force is not needed. For the intermediate values of $\bar{\alpha}_p(0.2<\bar{\alpha}_p<0.4)$, the function $h(\bar{\alpha}_p)$ reaches a maximum value. Thus, the maximum value of the drag correction coefficient occurs in this interval. The form suggested by (Parmentier et al., 2012) is also shown by Fig. 23. We recall that these authors performed the fully resolved simulation of gas–solid flow in a 2D dense fluidised bed. For the intermediate values of $\bar{\alpha}_p(0.2<\bar{\alpha}_p<0.35)$, both functions have the same values. For $\bar{\alpha}_p$ smaller than 0.2, fully developed 3D PCFB simulation shows less drag correction. This is reasonable as the gas passes through 3D meso-scale structures more easily than through 2D meso-scale structures. This is also discussed by Igci and Sundaresan (2011) for 2D and 3D flows in periodic domains. However, for values $\bar{\alpha}_p$ larger than 0.4, PCFB simulation shows a larger drag correction than that found by Parmentier et al. (2012). This probably occured because of an insufficient number of realisations in this interval. Therefore, we propose the following modification of Parmentier et al. (2012)'s function $h(\bar{\alpha}_p)$ for $\bar{\alpha}_p$ smaller than 0.2 as:

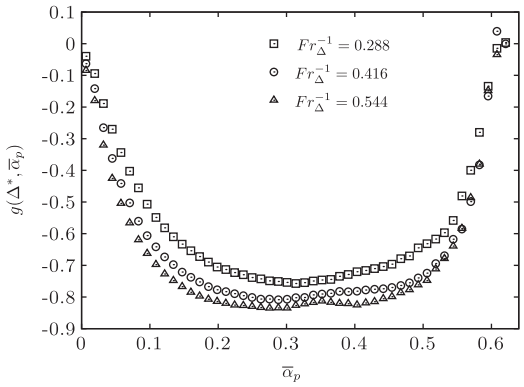

Fig. 22. The function $g(\Delta^*, \bar{\alpha}_p)$ for inverse Froude numbers $Fr_{\Delta}^{-1} = 0.288,\ 0.416$ and 0.544 based on the filter width $\overline{\Delta}$.

$$h(\bar{\alpha}_p) = -tanh\left(\frac{\bar{\alpha}_p}{C_{h,1}}\right)\sqrt{\frac{\bar{\alpha}_p}{\alpha_{p,max}}}\left(1-\frac{\bar{\alpha}_p}{\alpha_{p,max}}\right)^2 \times\left(1-C_{h,2}\frac{\bar{\alpha}_p}{\alpha_{p,max}}+C_{h,3}\left(\frac{\bar{\alpha}_p}{\alpha_{p,max}}\right)^2\right) \tag{29}$$

with constants $C_{h,1}$, $C_{h,2}$ and $C_{h,3}$ having the values 0.1, 1.88, 5.16, respectively. The maximum volume fraction of solid phase $\alpha_{p,max}$ is set to 0.64 and the function is shown by Fig. 24. After determination of the function $h(\bar{\alpha}_p)$, we calculate the function $f(\Delta^*)$ that can be evaluated by

$$f(\Delta^*) \equiv \frac{\overline{\left\langle \bar{\alpha}_p \widetilde{V}_{d,z} \right\rangle^{t,n}}}{\left\langle h(\bar{\alpha}_p)\bar{\alpha}_p(\widetilde{U}_{g,z}-\widetilde{U}_{p,z})\right\rangle^{t,n}} \tag{30}$$

for different filter widths $\overline{\Delta}$. The following form is proposed

$$f(\Delta^*) = \frac{\overline{\Delta}^{*2}}{C_{f,1}+\overline{\Delta}^{*2}} \tag{31}$$

with the constant $C_{f,1}$ equal to 0.15 and Δ^* given by

$$\Delta^* = \frac{\overline{\Delta}}{\tilde{\tau}_p|\widetilde{\mathbf{V}}_r|} \tag{32}$$

where $\tilde{\tau}_p$ is the filtered relaxation time, $|\widetilde{\mathbf{V}}_r|$ is the magnitude of the filtered relative velocity and $\overline{\Delta}$ is the filter width. The exact and proposed functions $f(\Delta^*)$ are shown by Fig. 25. It can expected that the clusters will not grow beyond some critical size and the effective drag coefficient will be independent of filter width when the latter is sufficiently large. For larger filter widths, the function $f(\Delta^*)$ reaches a constant value, which is equal to 1. Additionally, we note

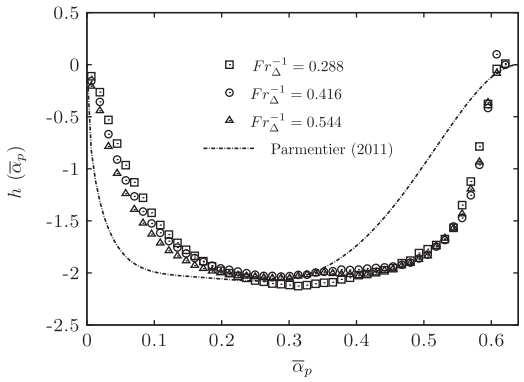

Fig. 23. The function $h(\bar{\alpha}_p)$ for inverse Froude numbers $Fr_{\Delta}^{-1} = 0.288,\ 0.416$ and 0.544 based on the filter width $\overline{\Delta}$.

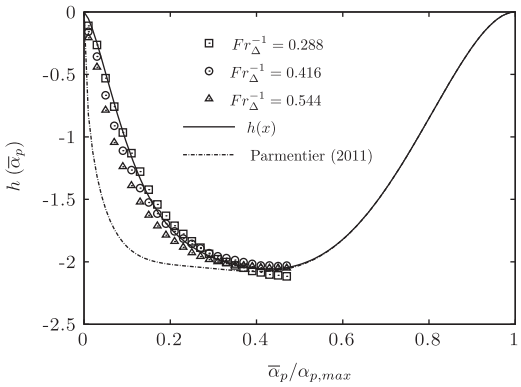

Fig. 24. The proposed function $h(\bar{\alpha}_p)$.

that the shape of the function $f(\Delta^*)$ could be sensitive to the filtering procedure and the numerical scheme of the solver.

The proposed model is constructed on the separation of the correlation of the gas velocity and the solid volume fraction by a correction, which is a the function of filtered solid volume fraction, filter width, filtered relative velocity, filtered relaxation time and the model constant $K_{\beta\beta}$. Most of industrial applications are conducted in channel flow and it is well known that the gas–solid flow is highly anisotropic. To take account the effect of anisotropy on the effective drag force into account, the dynamical adjustment proposed by Parmentier et al. (2012) is applied to calculate the model constant $K_{\beta\beta}$ depending on direction and flow (see Appendix C for the dynamic adjustment of the model constant $K_{\beta\beta}$). In addition, the dimensionless length scale of the model remains an open question. Parmentier et al. (2012) proposed the mesh dependency as a function of the bed length. Here, we propose the model as a function of the filtered relaxation time, filtered relative velocity and filter width. Mesh-independent results for different PCFB configurations, detailed in Section 2, will be used for further studies and the proposed methodology can be applied to validate studies of mesh dependency. It is worth noting that this model might be incapable of predicting a transient regime in circulating fluidised beds and the transient regime cannot be investigated by fully developed PFBC simulations.

5.2. Structural models

The proposed functional model has several parameters, such as the particle properties, the solid volume fraction and the filter size dependencies. These parameters were obtained by using a

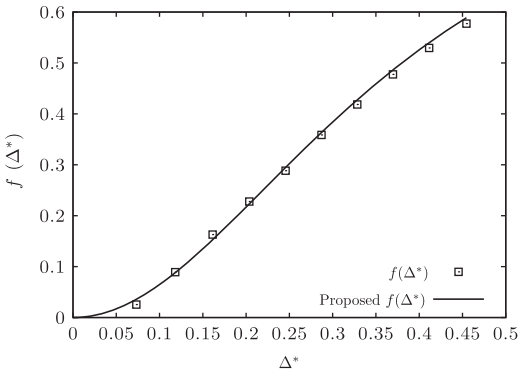

Fig. 25. The measured and proposed function $f(\Delta^*)$ where $\Delta^* = \overline{\Delta}/(\tilde{\tau}_p|\widetilde{\mathbf{V}}_r|)$ with the filtered relaxation time $\tilde{\tau}_p$, the magnitude of the filtered relative velocity $|\widetilde{\mathbf{V}}_r|$ and the filter width $\overline{\Delta}$.

particular fluidised bed and the predictability of the proposed model may be restricted for some applications. For of this reason, we looked for an alternative method, which led to some structural models. As has already mentioned, the interactions between resolved and unresolved scales has not been well established and, for structural models, it is not necessary to have prior knowledge of the nature of the interactions between the sub-grid scales (Sagaut, 2004).

5.2.1. Germano's decomposition

$\bar{\alpha}_p\widetilde{V}_{d,i}$ can be decomposed by following Germano (1986) as

$$\bar{\alpha}_p\widetilde{V}_{d,i} = \mathcal{L}_i + \mathcal{C}_i + \mathcal{R}_i \tag{33}$$

where the Leonard, $\mathcal{L}_i$, Cross, $\mathcal{C}_i$, and Reynolds, R_i, terms are defined by:

$$\mathcal{L}_i = \overline{\bar{\alpha}_p\widetilde{U}_{g,i}} - \bar{\bar{\alpha}}_p\widetilde{\bar{U}}_{g,i} \tag{34}$$

$$\mathcal{C}_i = \overline{\bar{\alpha}_p U''_{g,i}} - \bar{\bar{\alpha}}_p\widetilde{U''}_{g,i} + \overline{\alpha'_p\widetilde{U}_{g,i}} - \overline{\alpha'_p}\widetilde{\bar{U}}_{g,i} \tag{35}$$

$$\mathcal{R}_i = \overline{\alpha'_p U''_{g,i}} - \overline{\alpha'}_p\widetilde{U''}_{g,i} \tag{36}$$

with the fluctuation of volume fraction $\alpha'_p = \alpha_p - \bar{\alpha}_p$ and the fluctuation of the gas velocity $U''_{g,i} = U_{g,i} - \widetilde{U}_{g,i}$. The averages of the decompositions along the mean flow direction are shown by Fig. 26. Leonard terms are good approximations for $\bar{\alpha}_p\widetilde{V}_{d,z}$ up to $Fr_\Delta^{-1} = 0.16$. Between $Fr_\Delta^{-1} = 0.16$ and $Fr_\Delta^{-1} = 0.32$, $\bar{\alpha}_p\widetilde{V}_{d,z}$ can be represented by the sum of Leonard and Cross terms and Reynolds terms are negligible. However, Reynolds terms make the main contribution to $\bar{\alpha}_p\widetilde{V}_{d,z}$ for intermediate and larger filters $\left(Fr_\Delta^{-1} > 0.32\right)$. If Fr_Δ^{-1} is greater than 0.64, $\langle\mathcal{L}_z + \mathcal{C}_z\rangle$ reaches a constant value and $\langle\mathcal{R}_z\rangle$ increases linearly. Fig. 27 shows Reynolds terms along the mean flow and radial directions. Reynolds terms along the mean flow direction are one order greater than those in radial directions. Parmentier et al. (2012) performed a Taylor expansion of $\bar{\alpha}_p\widetilde{V}_{d,i}$ given by:

$$\bar{\alpha}_g\bar{\alpha}_p\widetilde{V}_{d,i} = \frac{\overline{\Delta}^2}{12}\frac{\partial\alpha_p}{\partial x_j}\frac{\partial U_{g,i}}{\partial x_j} \tag{37}$$

where 1/12 is a theoretical value and varies depending on the filter type. The derivation in this study was carried out by expanding series, with taking high order terms into account (for details, see Appendix D). $\bar{\alpha}_p\widetilde{V}_{d,i}$ can be modelled by

$$\bar{\alpha}_p\widetilde{V}_{d,i} = \frac{\overline{\Delta}^2}{12}\frac{\partial\alpha_p}{\partial x_j}\frac{\partial U_{g,i}}{\partial x_j} - \frac{\overline{\Delta}^4}{576}\frac{\partial^2\alpha_p}{\partial x_j x_k}\frac{\partial^2 U_{g,i}}{\partial x_j x_k} + \mathcal{O}(\overline{\Delta}^6) \tag{38}$$

The combination of Leonard, $\mathcal{L}_i$, and Cross, $\mathcal{C}_i$, terms leads to the first term on the right-hand side:

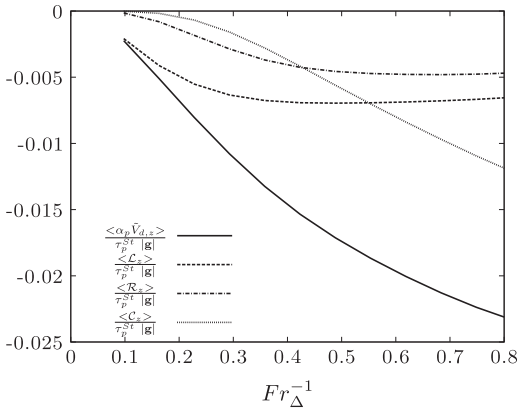

Fig. 26. Averaged Germano's decomposition terms along the mean flow direction for different inverse Froude numbers Fr_Δ^{-1} based on the filter width $\overline{\Delta}$.

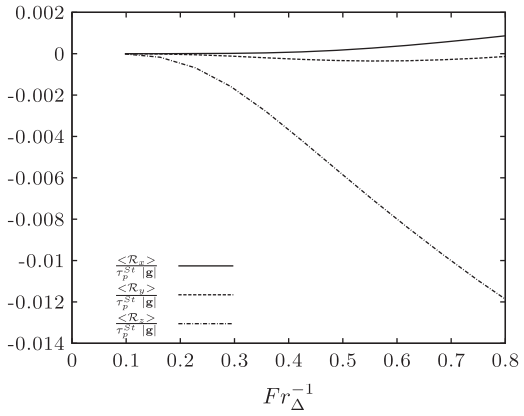

Fig. 27. Averaged Reynolds terms along the vertical ($z-$) and radial ($x-$,$y-$) directions for different inverse Froude numbers Fr_Δ^{-1} based on the filter width $\overline{\Delta}$.

$$\mathcal{L}_i + \mathcal{C}_i = \frac{\overline{\Delta}^2}{12}\frac{\partial\alpha_p}{\partial x_j}\frac{\partial U_{g,i}}{\partial x_j} \tag{39}$$

Eq. (39) is referred to as the Gradient model by analogy with single-phase turbulence modelling by Clark et al. (1979). The Reynolds terms $\mathcal{R}_i$ appear only as fourth-order terms:

$$\mathcal{R}_i = \frac{\overline{\Delta}^4}{576}\frac{\partial^2\alpha_p}{\partial x_j\partial x_k}\frac{\partial^2 U_{g,i}}{\partial x_j\partial x_k} \tag{40}$$

5.2.2. Gradient model (tensor diffusivity model)

By neglecting the fourth-order term, $\bar{\alpha}_p\widetilde{V}_{d,i}$ can be modelled by the following equation:

$$\bar{\alpha}_p\widetilde{V}_{d,i} = A_{jk}\overline{\Delta}^2\frac{\partial\bar{\alpha}_p}{\partial x_j}\frac{\partial\widetilde{U}_{g,i}}{\partial x_k} \tag{41}$$

A_{jk} is a second-order tensor dependent on filter type. This model shows good performance in terms of correlation coefficient, because it represents the first term in the Taylor series expansion. It is assumed that A_{jk} is diagonal ($A_{jk} = 0$ if $j \neq k$) and $A_{xx} = A_{yy} = \lambda A_{zz}$ in the specific frame where the mean flow direction ($z-$) is aligned with the direction of acceleration due to gravity. We propose a general form of the Gradient model as

$$\bar{\alpha}_p\widetilde{V}_{d,\beta} = A_{\beta\beta}\overline{\Delta}^2\frac{\partial\bar{\alpha}_p}{\partial x_j}\frac{\partial\widetilde{U}_{g,\beta}}{\partial x_j} \tag{42}$$

The model coefficients were determined using a least-squares method from the Euler–Euler DNS database. The model coefficient A_{zz} for mean flow direction is close to the theoretical value of 1/12 and model coefficients A_{xx}, A_{yy} for transverse and longitudinal directions increase linearly with filter width (see Fig. 28). Vreman et al. (1996) investigated the Gradient model for the turbulent stress tensor to see if it was applicable for compressible turbulent flows. It was revealed that the model gave rise to instabilities for a weakly compressible turbulent temporal mixing layer and led to a blowup in calculations. Vreman et al. (1996) performed a linear stability analysis of Burger's equation supplemented by the Gradient model to clarify the nature of the instability and showed that the growth-rate of the instability was infinite. Eyink (2006) pointed out that the deconvolution operator to re-build unresolved scales by a resolved field was unbounded in the natural function space for velocity and scalar fields. Vreman et al. (1996) added an eddy-viscosity part to stabilise the model. In the following section, we present an extension of this model taking the high-order terms into account. Another reason to extend the model is that the $\mathcal{O}(\overline{\Delta}^4)$ term is not small. For rapidly fluctuating variables, such as the solid

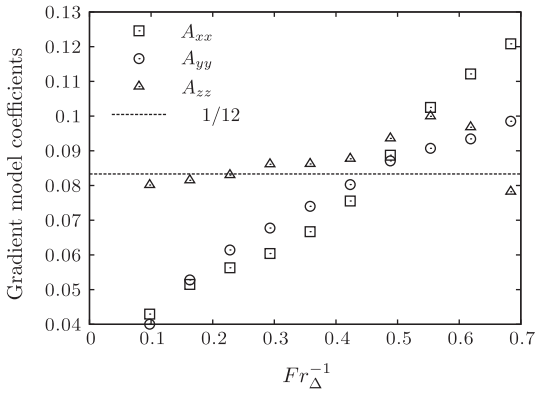

Fig. 28. Gradient model coefficients $A_{\beta\beta}$ along the vertical ($z-$) and radial ($x-$,$y-$) directions for different inverse Froude numbers Fr_{Δ}^{-1} based on the filter width $\overline{\Delta}$.

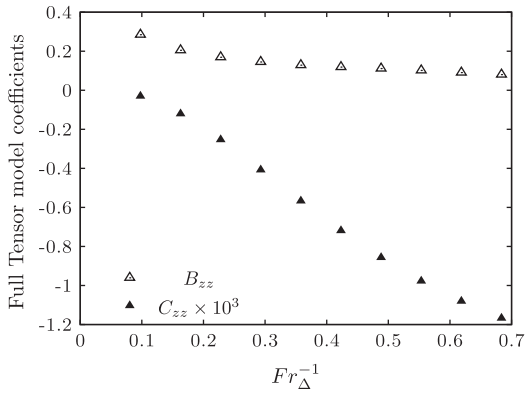

Fig. 29. Full Tensor model coefficients B_{zz} and C_{zz} along the mean flow for different inverse Froude numbers Fr_{Δ}^{-1} based on the filter width $\overline{\Delta}$.

volume fraction, this term cannot simply be omitted. As shown by Fig. 26, Reynolds terms of $\bar{\alpha}_p\widetilde{V}_{d,i}$ are dominant for large filter widths and therefore have to be taken into account. From the numerical point of view, the high-order term would preferably be $\mathcal{O}(\overline{\Delta}^4)$ but in practice, the high-order term is evaluated by $\mathcal{O}(\overline{\Delta}^2)$ when the numerical scheme produces the same order errors, which is the case for second-order accurate schemes.

5.2.3. Full Tensor model

From the consequences of Germano's decomposition (Fig. 26), it was pointed out that Reynolds term was significant for large filter widths. The Gradient model does not take this term into account by assuming that the resolution of the Leonard and Cross terms is sufficient for the modelling of the drag force sub-grid contribution. Following the analytical expansion, $\bar{\alpha}_p\widetilde{V}_{d,i}$ can be modelled as

$$\bar{\alpha}_p\widetilde{V}_{d,i} = B_{jk}\overline{\Delta}^2\frac{\partial\bar{\alpha}_p}{\partial x_j}\frac{\partial\widetilde{U}_{g,i}}{\partial x_k} + C_{jklm}\overline{\Delta}^4\frac{\partial^2\bar{\alpha}_p}{\partial x_j\partial x_k}\frac{\partial^2\widetilde{U}_{g,i}}{\partial x_l\partial x_m} \tag{43}$$

B_{jk} is a second-order tensor and C_{jklm} is the fourth-order tensor. They are dependent on filter type. We assume that B_{jk} and C_{jklm} are diagonal tensors and the Full Tensor model in general form can written

$$\bar{\alpha}_p\widetilde{V}_{d,\beta} = B_{\beta\beta}\overline{\Delta}^2\frac{\partial\bar{\alpha}_p}{\partial x_j}\frac{\partial\widetilde{U}_{g,\beta}}{\partial x_j} + C_{\beta\beta}\overline{\Delta}^4\frac{\partial^2\bar{\alpha}_p}{\partial x_j\partial x_k}\frac{\partial^2\widetilde{U}_{g,\beta}}{\partial x_j\partial x_k} \tag{44}$$

The constants $B_{\beta\beta}$ and $C_{\beta\beta}$ can be determined by performing multivariate linear regression. Let $\mathcal{E}_i$ be the error in Eq. (39)

$$\mathcal{E}_\beta = \sqrt{\bar{\alpha}_p\widetilde{V}_{d,\beta} - \left(B_{\beta\beta}\overline{\Delta}^2\mathcal{M}_\beta + C_{\beta\beta}\overline{\Delta}^4\mathcal{N}_\beta\right)} \tag{45}$$

where $\mathcal{M}_\beta = \frac{\partial\bar{\alpha}_p}{\partial x_j}\frac{\partial\widetilde{U}_{g,\beta}}{\partial x_j}$ and $\mathcal{N}_\beta = \frac{\partial^2\bar{\alpha}_p}{\partial x_j x_k}\frac{\partial^2\widetilde{U}_{g,\beta}}{\partial x_j x_k}$. $B_{\beta\beta}$, $C_{\beta\beta}$ can be obtained by setting $\partial\mathcal{E}_\beta/\partial M_\beta = 0$ and $\partial\mathcal{E}_\beta/\partial\mathcal{N}_\beta = 0$. The coefficients along the mean flow direction are shown by Fig. 29. As expected, values of C_{zz} are very small compared with B_{zz}, especially for small filter widths, and the constant B_{zz} is independent of filter width. C_{zz} is negative and increases dramatically with respect to the filter width.

5.2.4. Mixed model

In 5.1, we stated that $\bar{\alpha}_p\widetilde{V}_{d,i}$ could be predicted in terms of $\bar{\alpha}_p(\widetilde{U}_{g,i} - \widetilde{U}_{p,i})$ for large filter widths. Afterwards, the structural Gradient model was proposed and it was stated that the Gradient model predicted $\bar{\alpha}_p\widetilde{V}_{d,i}$ correctly on the basis of theoretical representations of the Leonard and Cross terms for small filter widths. Here, we present the Mixed model, which can be constructed to take advantages of both the above models. In the decomposition of $\bar{\alpha}_p\widetilde{V}_{d,i}$, the part representing Reynolds terms can be modelled by the functional model as

$$\bar{\alpha}_p\widetilde{V}_{d,\beta} = D_{\beta\beta}\overline{\Delta}^2\frac{\partial\bar{\alpha}_p}{\partial x_j}\frac{\partial\widetilde{U}_{g,\beta}}{\partial x_j} + E_{\beta\beta}h(\bar{\alpha}_p)\bar{\alpha}_p(\widetilde{U}_{g,\beta} - \widetilde{U}_{p,\beta}) \tag{46}$$

The constants D_{zz} and E_{zz} are shown by Fig. 30. D_{zz} is independent of filter width and close to the theoretical value 1/12. E_{zz} can be written as the function $f(\Delta^*)$. We formulate the following relation in order to obtain the Dynamic Mixed model:

$$\bar{\alpha}_p\widetilde{V}_{d,\beta} = \frac{\overline{\Delta}^2}{12}\frac{\partial\bar{\alpha}_p}{\partial x_j}\frac{\partial\widetilde{U}_{g,\beta}}{\partial x_j} + K_{\beta\beta}f(\Delta^*)h(\bar{\alpha}_p)\bar{\alpha}_p(\widetilde{U}_{g,\beta} - \widetilde{U}_{p,\beta}) \tag{47}$$

The model constant for the gradient part is assumed to be equal to the theoretical value 1/12 in all directions. This assumption is a good approximation as shown by Fig. 28. With this assumption, we do not need a second test filter to calculate the constant for the gradient part. The model constant $K_{\beta\beta}$ of the functional part is adjusted dynamically (see Appendix C.1).

5.2.5. Dynamic Structure model

In this part, we propose a new class of sub-grid scale model for $\bar{\alpha}_p\widetilde{V}_{d,i}$. The proposed model uses the sub-grid scalar variance as a part of the scaling factor and small-scale statistics are extrapolated to provide knowledge of large-scale fields. The following model is proposed

$$\bar{\alpha}_p\widetilde{V}_{d,i} = -C_{sgs}\frac{\overline{\alpha_p\alpha_p} - \bar{\alpha}_p\bar{\alpha}_p}{\bar{\alpha}_p}(\widetilde{U}_{g,i} - \widetilde{U}_{p,i}) \tag{48}$$

where $\overline{\alpha_p\alpha_p} - \bar{\alpha}_p\bar{\alpha}_p$ is the sub-grid variance of α_p at the grid level. The sub-grid scalar variance is also referred to as the scalar mixedness since it measures the degree of local non-homogeneity of the

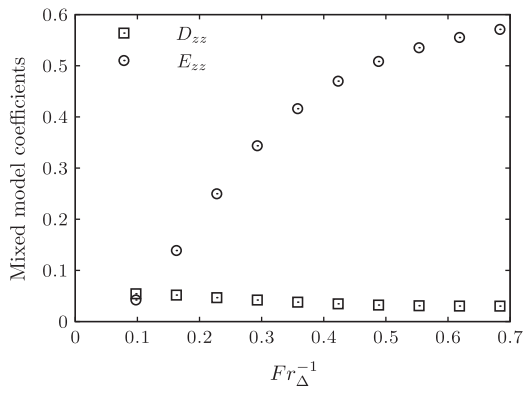

Fig. 30. Mixed model coefficients D_{zz} and E_{zz} along the mean flow for different inverse Froude numbers Fr_{Δ}^{-1} based on the filter width $\overline{\Delta}$.

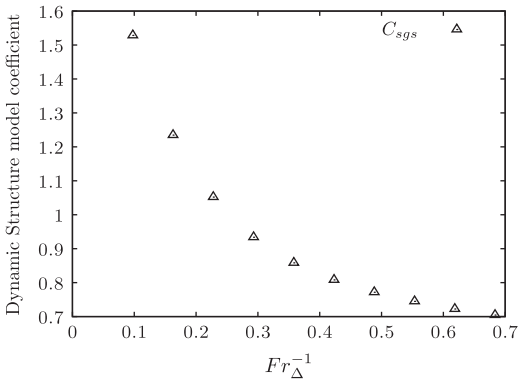

Fig. 31. Dynamic Structure model coefficient C_{sgs} along the mean flow for different inverse Froude numbers Fr_{Δ}^{-1} based on the filter width $\overline{\Delta}$.

solid volume fraction within the characteristic length. First, we calculated the correlation coefficient between $\bar{\alpha}_p \widetilde{V}_{d,i}$ and the predictions of the Dynamic Structure model. The model constant ranges from 1.5 to 0.8 (see Fig. 31). The sub-grid scalar cannot be found from the resolved field and we need a closure term or an additional transport equation for the sub-grid variance.

5.2.6. A priori analyses of effective drag model predictability

As a structural test of the models, r_i is computed as the correlation between the model predictions of and the measured $\bar{\alpha}_p \widetilde{V}_{d,i}$. Fig. 32 shows the correlation coefficients between the Smagorinsky-type, the Gradient, the Mixed, the Full Tensor, and the Dynamic Structure models, and the measured $\bar{\alpha}_p \widetilde{V}_{d,i}$ for different inverse Froude numbers Fr_{Δ}^{-1} based on the filter width $\overline{\Delta}$ along the x-direction. The Full Tensor model shows the poorest performance, with very low correlation coefficients ($-0.2 < r_x < 0.2$), while the Gradient model gives higher correlations (≈0.4). The correlation coefficients provided by the Smagorinsky-type, the Mixed and the Dynamic Structure models are moderate (≈0.5) for small filter widths. For large filter widths, the performances of these models are improved (≈0.6). Fig. 33 shows the correlation coefficients of the proposed models for different inverse Froude numbers Fr_{Δ}^{-1} based on the filter width $\overline{\Delta}$ along the y-direction. Model predictabilities are as similar as along the x-direction. Fig. 34 shows the correlation coefficients for different inverse Froude numbers Fr_{Δ}^{-1} based on the filter width $\overline{\Delta}$ along the z-direction. The Gradient model shows moderate performance (≈0.5) for small filter widths. However, the correlation coefficients provided by the Gradient

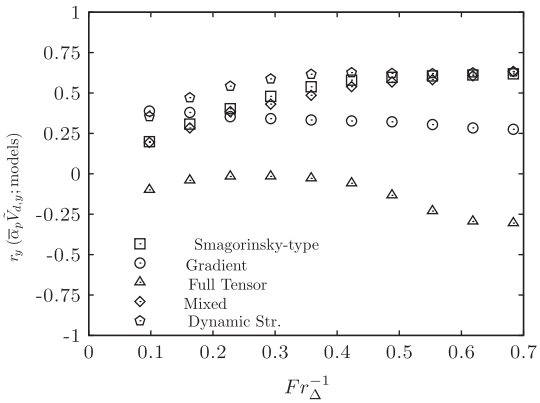

Fig. 33. Correlation coefficients r_y between the y-component of measured and modelled $\bar{\alpha}_p \widetilde{V}_{d,\beta}$ for different inverse Froude numbers Fr_{Δ}^{-1} based on the filter width $\overline{\Delta}$. The test filter width is $\widehat{\Delta} = \sqrt{5}\overline{\Delta}$ by following Lilly (1992).

model become smaller as filter width increases. For large filter widths, the correlation coefficients are around 0.3. It was expected that Reynolds terms would be dominant for large filter widths and that the Gradient model would cancel out these contributions. In order to improve the predictability of the Gradient model, Reynolds terms modelled by high-order derivatives were introduced by the Full Tensor model. We did not see any improvement in terms of the correlation coefficients. The Dynamic Structure model provides higher correlations (≈0.8) independent of filter widths and the Smagorinsky-type and the Mixed models provide moderate correlation coefficients (≈0.6) for small filter sizes and high correlation coefficients (≈0.8) for intermediate and large filter widths.

Fig. 35 shows pdfs of relative error, defined as in Eq. (20), of $\bar{\alpha}_p \widetilde{V}_{d,i}$ for all the models along the mean flow direction for inverse Froude number $Fr_{\Delta}^{-1} = 0.352$ on the filter width $\overline{\Delta}$. Statistically, these models predict comparable magnitudes of $\bar{\alpha}_p \widetilde{V}_{d,i}$. The pdf of relative error for the Smagorinsky-type model shows that there is a mismatch with the predicted $\bar{\alpha}_p \widetilde{V}_{d,i}$ due to the peak not being centred at zero. Fig. 36 shows pdfs of relative error, defined as in Eq. (28), of effective drag correction for all the models along the mean flow direction for inverse Froude number $Fr_{\Delta}^{-1} = 0.352$ based on the filter width. The Smagorinsky-type and the Dynamic Structure models can predict the correction very well along the mean direction. The mean squared errors E_i, calculated as in Eq. (21), are shown by Figs. 37–39. The Full Tensor model was found to have the highest mean squared error for all filter widths and all

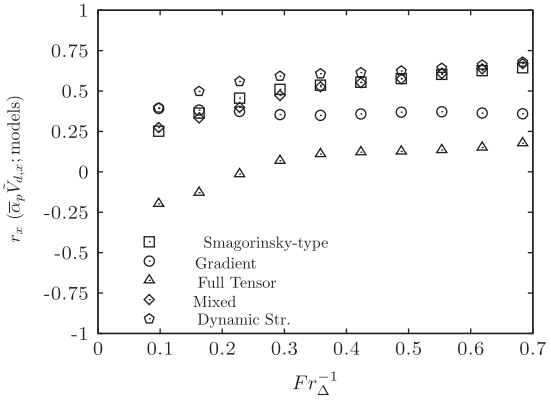

Fig. 32. Correlation coefficients r_x between the x-component of measured and modelled $\bar{\alpha}_p \widetilde{V}_{d,\beta}$ for different inverse Froude numbers Fr_{Δ}^{-1} based on the filter width $\overline{\Delta}$. The test filter width is $\widehat{\Delta} = \sqrt{5}\overline{\Delta}$ by following Lilly (1992).

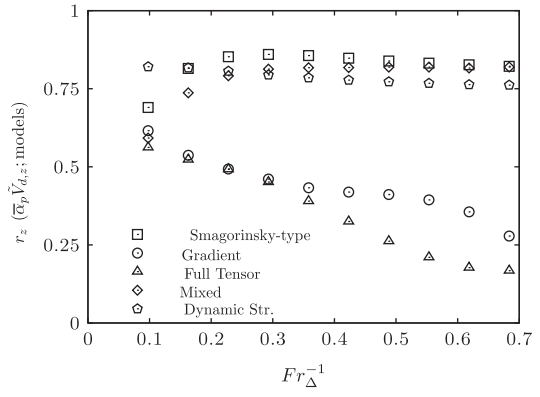

Fig. 34. Correlation coefficients r_z between the z-component of measured and modelled $\bar{\alpha}_p \widetilde{V}_{d,\beta}$ for different inverse Froude numbers Fr_{Δ}^{-1} based on the filter width $\overline{\Delta}$. The test filter width is $\widehat{\Delta} = \sqrt{5}\overline{\Delta}$ by following Lilly (1992).

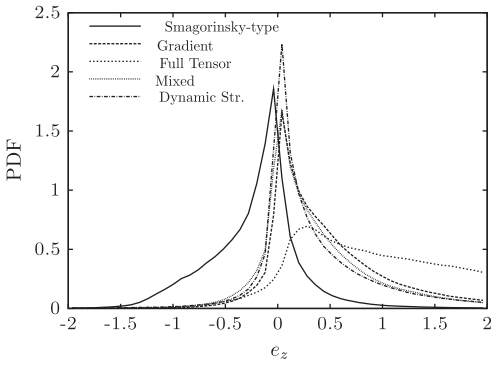

Fig. 35. Pdfs of relative error e_z, computed as in Eq. (20), for inverse Froude number $Fr_{\Delta}^{-1} = 0.352$ along the mean flow direction. The test filter width is $\widehat{\Delta} = \sqrt{5}\overline{\Delta}$ by following Lilly (1992).

directions while the Dynamic Structure model had the lowest values for radial directions. The Smagorinsky-type model had the lowest mean squared error along the mean flow direction.

6. Particle SGS stress tensor models

The particle sub-grid stress tensor $\sigma_{p,ij}^{sgs}$ is defined in the filtered momentum equation of the particulate phase as

$$\sigma_{p,ij}^{sgs} = \widetilde{U_{p,i}U_{p,j}} - \widetilde{U}_{p,i}\widetilde{U}_{p,j} \tag{49}$$

A priori analyses on SGS stress tensor show that the sub-grid correlated energy and the dissipation have to be modelled. Moreau et al. (2009) proposed dividing the particle sub-grid stress tensor $\sigma_{p,ij}^{sgs}$ into deviatoric and spherical parts in the framework of dilute particle laden turbulent flow modelling. Following Moreau et al. (2009), the Smagorinsky (1963) model is proposed for the deviatoric part here and the Yoshizawa (1986) model is used for the spherical part as follows:

$$\sigma_{p,ij}^{sgs} = \sigma_{p,ij}^{*} + \frac{1}{3}\sigma_{p,kk}\delta_{ij} \tag{50}$$

$$= -C_s^2\overline{\Delta}^2\left|\widetilde{S}_p^*\right|\widetilde{S}_{p,ij}^* + \frac{2}{3}C_Y\overline{\Delta}^2\left|\widetilde{S}_p^*\right|^2\delta_{ij} \tag{51}$$

where $\widetilde{S}_{p,ij}^*$ is the trace free strain rate tensor of the filtered particle velocity and is given by

$$\widetilde{S}_{p,ij}^* = \frac{\partial\widetilde{U}_{p,i}}{\partial x_j} + \frac{\partial\widetilde{U}_{p,j}}{\partial x_i} - \frac{2}{3}\frac{\partial\widetilde{U}_{p,k}}{\partial x_k}\delta_{ij} \tag{52}$$

$\left|\widetilde{S}_p^*\right|$ is the norm of $\widetilde{S}_{p,ij}^*$ and defined by $\left|\widetilde{S}_p^*\right|^2 = 1/2\widetilde{S}_{p,ij}^*\widetilde{S}_{p,ij}^*$. The modelling form chosen is consistent with what has been done in

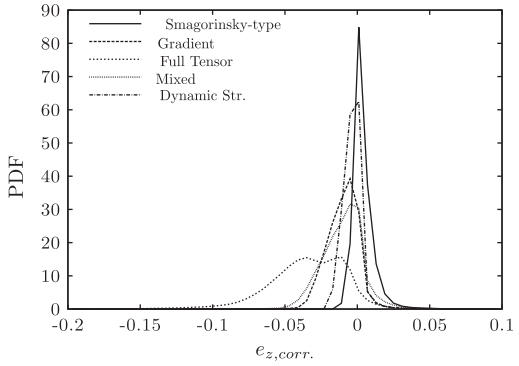

Fig. 36. Pdfs of relative error e_z of the drag correction, computed as in Eq. (20), for inverse Froude number $Fr_{\Delta}^{-1} = 0.352$ along the mean flow direction. The test filter width is $\widehat{\Delta} = \sqrt{5}\overline{\Delta}$ by following Lilly (1992).

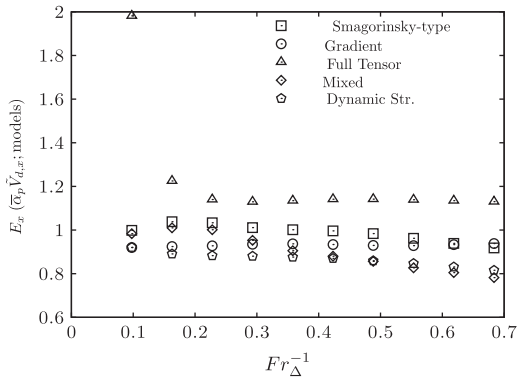

Fig. 37. Mean squared error E_x, computed as in Eq. (21), for the x-component of measured and modelled $\overline{\alpha}_p\widetilde{V}_{d,\beta}$ for different inverse Froude numbers Fr_{Δ}^{-1} based on the filter width $\overline{\Delta}$. The test filter width is $\widehat{\Delta} = \sqrt{5}\overline{\Delta}$ by following Lilly (1992).

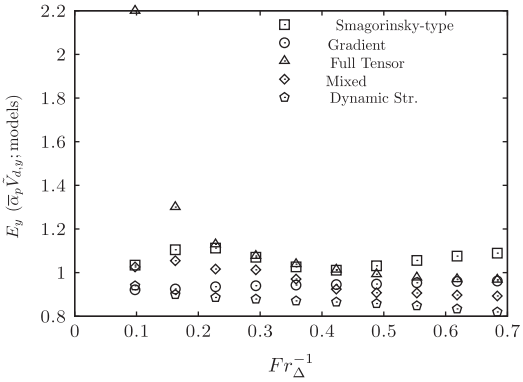

Fig. 38. Mean squared error E_y, computed as in Eq. (21), for the y-component of measured and modelled $\overline{\alpha}_p\widetilde{V}_{d,\beta}$ for different inverse Froude numbers Fr_{Δ}^{-1} based on the filter width $\overline{\Delta}$. The test filter width is $\widehat{\Delta} = \sqrt{5}\overline{\Delta}$ by following Lilly (1992).

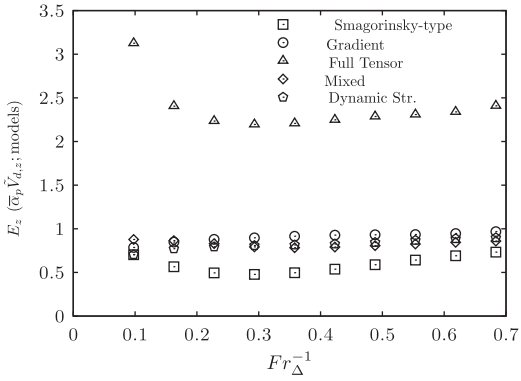

Fig. 39. Mean squared error E_z, computed as in Eq. (21), for the z-component of measured and modelled $\overline{\alpha}_p\widetilde{V}_{d,\beta}$ for different inverse Froude numbers Fr_{Δ}^{-1} based on the filter width $\overline{\Delta}$. The test filter width is $\widehat{\Delta} = \sqrt{5}\overline{\Delta}$ by following Lilly (1992).

single-phase turbulence. Agrawal et al. (2001) argued that sub-grid viscosity was proportional to macro-scale strain rate in single-phase turbulent flow while, in this problem, it appears to be inversely proportional to strain rate.

6.1. Assessment of Smagorinsky and Yoshizawa models

The models are assessed at the tensor and scalar levels. At scalar level, the sub-grid tensor is multiplied by the gradient of filtered

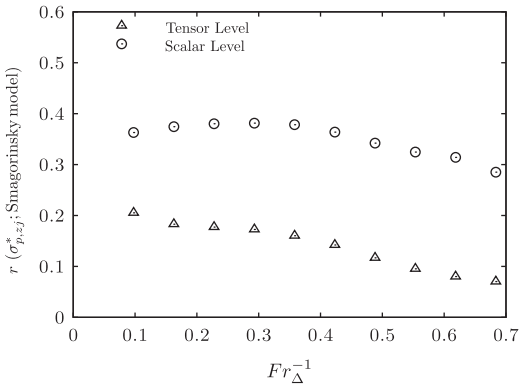

Fig. 40. Correlation coefficients r between the deviatoric part of the filtered particle sub-grid stress tensor $\sigma^*_{p,zj}$ and Smagorinsky model for different inverse Froude numbers Fr_Δ^{-1} based on the filter width $\overline{\Delta}$ at the tensor and scalar level.

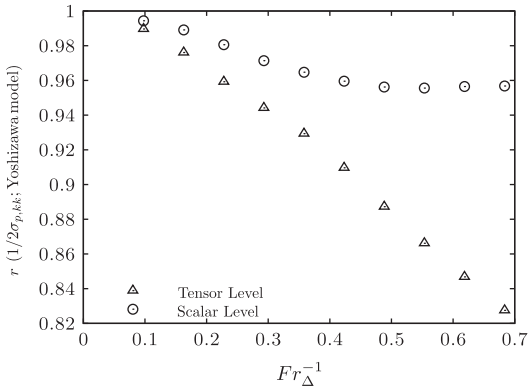

Fig. 41. Correlation coefficients r between the filtered particle sub-grid energy $1/2\sigma_{p,kk}$ and Yoshizawa model for different inverse Froude numbers Fr_Δ^{-1} based on the filter width $\overline{\Delta}$ at the tensor and scalar level.

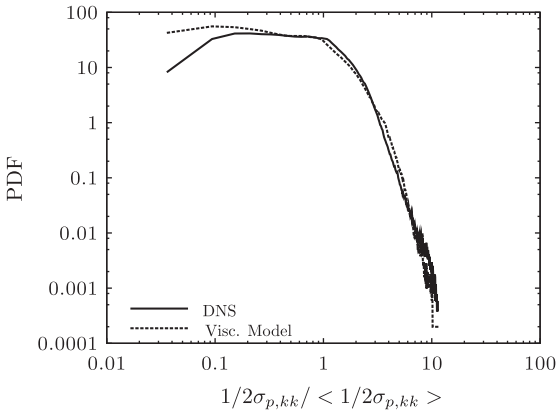

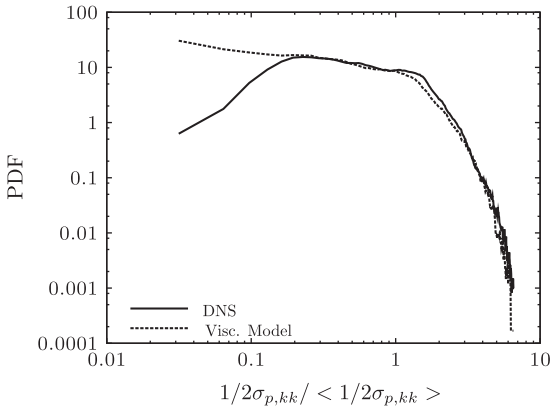

Fig. 42. Pdfs of particle sub-grid energy $1/2\sigma_{p,kk}$ from DNS data and by the Yoshizawa model for inverse Froude numbers $Fr_\Delta^{-1} = 0.224$ and 0.480.

particle velocities. The correlation coefficients between the deviatoric part of the filtered particle sub-grid stress tensor $\sigma^*_{p,zj}$ and the Smagorinsky model are shown by Fig. 40. The Smagorinsky model performs poorly in terms of the correlation coefficients ($r \sim 0.2$) at the tensor level. It is well established the dissipation characteristics of the Smagorinsky model, and thus the correlation coefficients between the product of the deviatoric part of the tensor by the gradients of the filtered particles velocities and of the Smagorinsky model prediction are also presented (see Fig. 40). The model shows better performance at the scalar level than at the tensor level ($r \sim 0.4$).

Fig. 41 shows the correlation coefficients between the particle sub-grid energy $1/2\sigma_{p,kk}$ and predictions by the Yoshizawa model. The Yoshizawa model predicts the compression stress of particle phases very well and the correlation coefficients are really high for the tensor level. For the scalar level, the correlation coefficients are up to 0.95 even for larger filter sizes. PDFs of the sub-grid energy and dissipation are compared with the predictions of viscosity models (Smagorinsky, Yoshizawa model) are shown by Figs. 42 and 43. The Yoshizawa model overestimates the level of the sub-grid energy at its lows values. This poor prediction can be seen easily seen for $Fr_\Delta^{-1} = 0.48$. The PDF of sub-grid dissipation $\sigma^*_{p,zj}\frac{\partial \widetilde{U}_{p,zj}}{\partial x_j}$ has some negative values, which represent the backscatter effect. However, it is well known that the Smagorinsky model is not able to resolve this backscatter and underestimation of dissipation occurs for every filter size consistent with correlation coefficients, as shown previously.

The viscosity model constants C_s and C_Y calculated from DNS results by the least square method are shown by Fig. 44. C_s was calculated by following the procedure for the dynamic Smagorinsky model (Germano et al., 1991) for single-phase turbulent flow along the homogeneous direction. C_s is smaller than single-phase flow model constants ([0.1, 0.2] for homogeneous isotropic turbulence, 0.079 channel flow). C_Y are independent for small and intermediate filter sizes and can be evaluated to be approximately 0.05. For large filter widths, C_Y increases linearly and this trend has to be validated in the PCFB with longer length. Moreau et al. (2009) estimated 0.051 from DNS simulation of homogeneous isotropic turbulence in the framework of the mesoscopic Eulerian approach. Erlebacher et al. (1992) have performed direct simulations of compressible homogeneous turbulence at Mach numbers ranging from 0.1 to 0.6 with the Yoshizawa model and they evaluated C_Y at 0.0066. This value was determined with a linear least-squares regression method at the vector level and it was stated that it depended on the Mach number. Additionally, Zang et al. (1991) studied the influence of this constant in LES of compressible homogeneous decaying turbulence at a turbulent Mach number of 0.1. C_Y varied from its standard value (0.0066) to a value 50 times larger. Here, we calculated a value 25 times larger than the standard for single-phase flow and this could be a result of the high compressibility of the dispersed phase. Additionally, C_Y could be dependent on the particle inertia characterised by the dimensionless Stokes number $\tilde{\tau}_p \left|\widetilde{S}^*_{p,ij}\right|$.

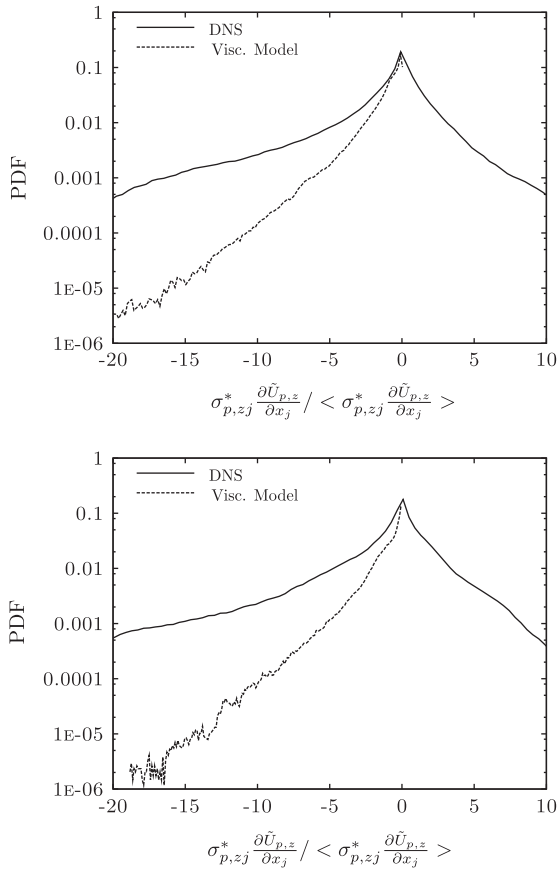

Fig. 43. Pdfs of particle sub-grid dissipation from DNS data and by the Smagorinsky model for inverse Froude numbers $Fr_{\Delta}^{-1} = 0.224$ and 0.480.

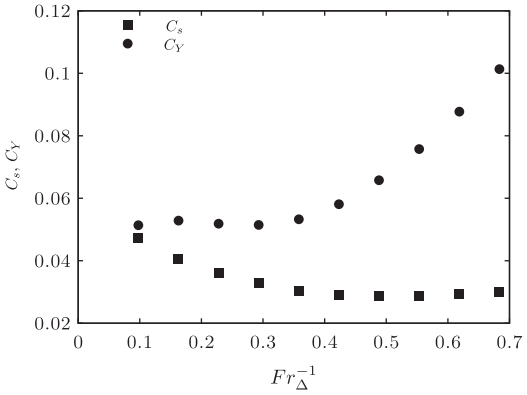

Fig. 44. Yoshizawa and Smagorinsky model coefficients, C_Y and C_s, respectively, for different inverse Froude numbers Fr_{Δ}^{-1} based on the filter width $\overline{\Delta}$.

7. Conclusion

Meso-scale structures are continuously formed in a circulating fluidised bed and they can be resolved through the Eulerian approach by supplementing the kinetic theory of granular flows on a high-resolution computational grid. However, simulations with mesh sizes larger than the small-scale structure size cancel out these structures and this causes poor predictions of bed hydrodynamics.

To investigate the effects of unresolved structures on the resolved field, we first obtained mesh-independent results for gas–solid in the 3D periodic circulating fluidised bed. Then, we used these results in a systematic approach based on *a priori* methodology. We performed the filtering procedure on a given Euler–Euler model and obtained the filtered momentum and filtered particle agitation transport equations. Additional terms arising from to the filtering procedure were investigated by budget analyses to determine their importance. It was found that meso-scale structures affected the flow characteristics profoundly. In particular, cancellation of these structures led to an overestimation of the drag force between gas and particle phases. We showed that the sub-grid drift velocity, defined as the difference between the filtered gas velocity seen by the particulate phase and the filtered gas velocity, had to be modelled to obtain the correct drag.

Some families of functional and structural models were proposed for sub-grid drift velocity and the models' predictions were tested in an *a priori* manner with correlation coefficients, mean squared error and probability density functions of local relative error. For the functional model, the Smagorinsky-type model was proposed as a continuation of the work of Parmentier et al. (2012). The solid volume fraction dependency of the model was given by the function $h(\bar{\alpha}_p)$. The shape of this function obtained from the high resolution 2D simulation of dense fluidized bed by Parmentier et al. (2012), was improved by the high-resolution 3D simulation of dilute gas–solid flow in the periodic circulating fluidised bed. The function $h(\bar{\alpha}_p)$ obtained from the high-resolution simulation of the periodic circulating fluidised bed shows less drag correction for the case of a solid volume fraction smaller than 0.2. This result has an obvious physical meaning since gas passes through 3D structures more easily than through 2D structures.

The mesh-dependency of the functional model was defined by the filter width, the filtered relative velocity and the filtered relaxation time. As structural models, we proposed the Gradient, the Full Tensor, the Mixed and the Dynamic Structure model. The Gradient model, which considers only the Leonard and Cross terms of Germano's decomposition of $\bar{\alpha}_p \tilde{V}_{d,i}$, showed good performance in terms of correlation coefficient for small filter widths. We introduced the high-order terms, which are fourth order of the filter width, to take Reynolds terms into account. The Mixed model was proposed where high-order terms were modelled by the functional model (Smagorinsky-type model). We obtained high correlation coefficients even for large filter widths. Sub-grid structure properties were transferred to the resolved field by introducing the sub-grid scalar variance of the solid volume fraction in the Dynamic Structure model. It gave high correlation coefficients independent of filter widths.

Filtering meso-scale structures yielded to SGS stress tensors which increased the effective viscosity and normal stresses of the particulate phase. The Smagorinsky model, as used in single-phase turbulent flow, was used to model the effective viscosity but it shows poor performance in terms of correlation coefficient. The model constant of the Smagorinsky model was smaller than that of single-phase turbulent flows. The Yoshizawa model was used to close the sub-grid correlated energy and its predictions were higher. The model coefficient of the Yoshizawa model was consistent with previous applications for Large Eddy Simulation of turbulent dilute gas-solid flow. We also performed a budget analysis of the filtered transport equation of particle agitation and demonstrated that the production of the particle agitation was underestimated at increasing filter width.

In this study, we have explored different models for the effective drag force and identified the strengths and limitations of each of them. The Dynamic Functional model is the most reliable model for a structured grid and simplified computational domain but the mesh dependency of this model may be retuned either through larger-scale simulations or comparisons with experimental data. The Mixed model without dynamic adjustment of the model constant

is mostly suitable for simulations with unstructured mesh and complex geometries. Additionally, we examined the SGS particle stress term and constructed the model as in Large Eddy Simulation of turbulent flows. This approach was firstly used for gas–solid flows in circulating fluidised beds and, in terms of *a priori* performance, appears favourable for industrial applications. A further study could perform *a posteriori* tests and make comparisons between the predictions of the models and models already availabl (Igci and Sundaresan, 2011; Parmentier et al., 2012) for gas–solid flows in the 3D periodic circulating fluidised bed and available experimental data.

The polydisperse gas–solid flow modelling by an Euler–Euler approach could be addressed in a future study. For polydisperse gas–solid flows, the inter-particle interactions are taken into account by an additional term in the particulate momentum equations. The effect of mesh resolution on this term and the sub-grid scale modelling will be obtained by applying the proposed methodology from the present study.

Acknowledgements

This work was granted access to the HPC resources of CALMIP under allocation P0111 (Calcul en Midi- Pyrénées). This work was performed using HPC resources from GENCI-CINES (Grant 2012-x2012026012).

Appendix A. Mathematical modelling

The modelling approach is based on the Euler–Euler model formalism, which involves separate mean transport equations of mass, momentum and energy for the gas and particulate phases. The mass balance equation of each phase is (when subscript $k = g$, we refer to the gas and, when $k = p$ to the particulate phase)

$$\frac{\partial}{\partial t}(\alpha_k\rho_k)+\frac{\partial}{\partial x_i}(\alpha_k\rho_k U_{k,i})=0 \tag{A.1}$$

with α_k the volume fraction, ρ_k the density and U_k the mean velocity of phase k. The momentum balance equation of each phase is given by

$$\frac{\partial}{\partial t}\rho_k\alpha_k U_{k,i}+\frac{\partial}{\partial x_j}\rho_k\alpha_k U_{k,i}U_{k,j}=-\alpha_k\frac{\partial P_g}{\partial x_i}+I_{k,i}-\frac{\partial \Sigma_{k,ij}}{\partial x_j}+\alpha_k\rho_k g_i \tag{A.2}$$

with P_g the mean gas pressure, g_i the gravity acceleration, $\Sigma_{k,ij}$ the effective stress tensor, and $I_{k,i}$ the mean momentum transfer rate between phases without the mean gas pressure effect. The term $I_{k,i}$ is modelled by considering only the drag force between phases with the mean particle relaxation time scale τ_p,

$$I_{g,i}=-I_{p,i}=\frac{\alpha_p\rho_p}{\tau_p}V_{r,i} \quad \text{with} \quad \begin{cases} \tau_p=\frac{4}{3}\frac{\rho_p}{\rho_g}\frac{d_p}{C_D|\mathbf{v}_r|} \\ C_D=\frac{24}{Re_p}\left[1+0.15Re_p^{0.687}\right]\alpha_g^{-1.7} \\ Re_p=\frac{d_p|\mathbf{v}_r|}{v_g} \end{cases} \tag{A.3}$$

The mean drag coefficient C_D is written as a function of a particle Reynolds number from Wen and Yu (1966) with the mean particle Reynolds number Re_p. In (A.3), d_p is the particle diameter and v_g the molecular kinematic viscosity of the gas. The local instantaneous relative velocity $v_{r,i}$ is equal to the difference between the local particle velocity $u_{p,i}$ and the instantaneous gas velocity $\tilde{u}_{g,i}$ locally undisturbed by the presence of the particle. Finally, $V_{r,i}$ is the mean fluid-particle relative velocity, $V_{r,i} = U_{p,i} - U_{g,i}$.

The particulate stress tensor $\Sigma_{p,ij}$ is defined by

$$\Sigma_{p,ij}=\left[P_p-\lambda_p\frac{\partial U_{p,m}}{\partial x_m}\right]\delta_{ij}-\mu_p\left[\frac{\partial U_{p,j}}{\partial x_i}+\frac{\partial U_{p,i}}{\partial x_j}-\frac{2}{3}\delta_{ij}\frac{\partial U_{p,m}}{\partial x_m}\right] \tag{A.4}$$

with the collisional pressure, P_p, the bulk viscosity, λ_p, the restitution coefficient, e_c, that determines energy loss during inter-particle collisions, the pair correlation function, g_0, the particle agitation, q_p^2, and the shear viscosity, μ_p. These terms are

$$P_p=\alpha_p\rho_p\left[1+2\alpha_p g_0(1+e_c)\right]\frac{2}{3}q_p^2$$

$$g_0=\left(1-\frac{\alpha_p}{\alpha_{p,max}}\right)^{-2.5\alpha_{p,max}} \quad \text{where } \alpha_{p,max}=0.64$$

$$\lambda_p=\frac{4}{3}\alpha_p^2\rho_p d_p g_0(1+e_c)\sqrt{\frac{2}{3}\frac{q_p^2}{\pi}}$$

$$\mu_p=\alpha_p\rho_p\left[v_p^{kin}+v_p^{coll}\right]$$

$$v_p^{kin}=\frac{1}{2}\tau_p\frac{2}{3}q_p^2(1+\alpha_p g_0\Phi_c)\Big/\left[1+\frac{\tau_p}{2}\frac{\sigma_c}{\tau_c}\right]$$

$$v_p^{coll}=\frac{4}{5}\alpha_p g_0(1+e_c)\left[v_p^{kin}+d_p\sqrt{\frac{2}{3}\frac{q_p^2}{\pi}}\right]$$

The transport equation for particle agitation q_p^2 was developed in the framework of the kinetic theory of granular media supplemented by the interstitial fluid effect (Boëlle et al., 1995; Balzer et al., 1995; Gobin et al., 2003). The transport equation for particle agitation q_p^2 is

$$\frac{\partial}{\partial t}\alpha_p\rho_p q_p^2+\frac{\partial}{\partial x_i}\alpha_p\rho_p U_{p,i}q_p^2=\frac{\partial}{\partial x_i}\left[\alpha_p\rho_p\left(K_p^{kin}+K_p^{coll}\right)\frac{\partial q_p^2}{\partial x_i}\right]-\Sigma_{p,ij}\frac{\partial U_{p,i}}{\partial x_j}-\frac{1}{3}(1-e_c^2)\frac{\alpha_p\rho_p}{\tau_c}q_p^2-2\frac{\alpha_p\rho_p}{\tau_p}q_p^2 \tag{A.5}$$

The first term on the right-hand side in Eq. (A.5) represents the diffusive transport of q_p^2 by kinematic motion and collisions. The second term represents the production rate of q_p^2 by the mean particle velocity gradients. The third and fourth terms are the dissipation of q_p^2 through inelastic collisions and interaction with the gas phase, respectively. Eq. (A.5) is additionally solved with K_p^{kin}, K_p^{coll} and τ_c the kinematic diffusivity, the collisional diffusivity and the collision time as defined by

$$K_p^{kin}=\frac{5}{9}\tau_p\frac{2}{3}q_p^2(1+\alpha_p g_0\varphi_c)\Big/\left[1+\frac{5}{9}\tau_p\frac{\xi_c}{\tau_c}\right]$$

$$K_p^{coll}=\alpha_p g_0(1+e_c)\left[\frac{6}{5}K_p^{kin}+\frac{4}{3}d_p\sqrt{\frac{2}{3}\frac{q_p^2}{\pi}}\right]$$

$$\tau_c=\frac{d_p}{24\alpha_p g_0}\sqrt{\frac{3}{2}\frac{\pi}{q_p^2}}$$

respectively. Model coefficients are

$$\varphi_c=\frac{3}{5}(1+e_c)^2(2e_c-1)$$

$$\xi_c=\frac{1}{100}(1+e_c)(49-33e_c)$$

$$\sigma_c=\frac{1}{5}(1+e_c)(3-e_c)$$

$$\Phi_c=\frac{2}{5}(1+e_c)(3e_c-1)$$

Appendix B. Derivation of filtered Euler–Euler two-phase model

Let $\alpha_k(\mathbf{x},t)$ denote the volume fraction of phase k at location $\mathbf{x}$ and time t obtained by solving the Euler–Euler two-phase model equations. We can define the filtered phase volume fraction as

$$\bar{\alpha}_k(\mathbf{x},t)=\int\int\int \alpha_k(\mathbf{r},t)G(\mathbf{r}-\mathbf{x})d\mathbf{r} \tag{B.1}$$

where $G(\mathbf{r}-\mathbf{x})$ is a weight function that satisfies $\int\int\int G(\mathbf{r})d\mathbf{r}=1$. The filtered phase velocity of phase k is defined as

$$\widetilde{U}_k(\mathbf{x},t)=\frac{1}{\bar{\alpha}_k}\int\int\int G(\mathbf{r}-\mathbf{x})\alpha_k(\mathbf{r},t)U_k(\mathbf{r},t)d\mathbf{r} \tag{B.2}$$

Applying such a filter to the mass balance equation for the phase k, we obtain

$$\frac{\partial}{\partial t}\bar{\alpha}_k\rho_k+\frac{\partial}{\partial x_j}\rho_k\bar{\alpha}_k\widetilde{U}_{k,j}=0 \tag{B.3}$$

This filtering procedure can be applied to momentum balance. The filtered momentum balance of phase k is

$$\begin{aligned}\frac{\partial}{\partial t}\rho_k\bar{\alpha}_k\widetilde{U}_{k,i}+\frac{\partial}{\partial x_j}\rho_k\bar{\alpha}_k\widetilde{U}_{k,i}\widetilde{U}_{k,j}=&-\bar{\alpha}_k\frac{\partial\overline{P}_g}{\partial x_i}-\varphi^{sgs}_{k,i}+\widetilde{I}_{k,i}+I^{sgs}_{k,i}\\&-\frac{\partial}{\partial x_j}\widetilde{\Sigma}_{k,ij}-\frac{\partial}{\partial x_j}\Sigma^{sgs}_{k,ij}\\&-\frac{\partial}{\partial x_j}\rho_k\bar{\alpha}_k\sigma^{sgs}_{k,ij}+\bar{\alpha}_k\rho_k g_i\end{aligned} \tag{B.4}$$

Terms with superscript $(\cdot^{sgs})$ in Eq. (B.4) appear from the filtering process and they represent the interaction between filtered and sub-grid contributions. The term $\varphi^{sgs}_{k,i}$ represents the correlation between the volume fraction of the phase k and gas pressure

$$\varphi^{sgs}_{k,i}=\overline{\alpha_k\frac{\partial P_g}{\partial x_i}}-\bar{\alpha}_k\frac{\partial\widetilde{P}_g}{\partial x_i} \tag{B.5}$$

A Reynolds stress contribution coming from the gas or particle phase velocity fluctuations $\sigma^{sgs}_{k,ij}$ is defined by the following equation:

$$\sigma^{sgs}_{k,ij}=\widetilde{U_{k,i}U_{k,j}}-\widetilde{U}_{k,i}\widetilde{U}_{k,j} \tag{B.6}$$

The terms $\widetilde{I}_{k,i}$ and $I^{sgs}_{k,i}$ are the filtered and sub-grid contribution of the drag term and are defined as

$$\widetilde{I}_{g,i}=-\widetilde{I}_{p,i}=\frac{\bar{\alpha}_p\rho_p}{\tilde{\tau}_p}\left(\widetilde{U}_{p,i}-\widetilde{U}_{g,i}\right) \tag{B.7}$$

$$I^{sgs}_{g,i}=-I^{sgs}_{p,i}=\overline{\frac{\alpha_p\rho_p}{\tau_p}V_{r,i}}-\frac{\bar{\alpha}_p\rho_p}{\tilde{\tau}_p}\left(\widetilde{U}_{p,i}-\widetilde{U}_{g,i}\right) \tag{B.8}$$

In this study, we focus on the effective stress tensor of the particulate phase. The terms $\widetilde{\Sigma}_{p,ij}$ and $\Sigma^{sgs}_{p,ij}$ are the filtered and sub-grid contributions of the particulate stress tensor. These contributions are

$$\widetilde{\Sigma}_{p,ij}=\left(\widetilde{P}_p-\tilde{\lambda}_p\frac{\partial\widetilde{U}_{p,m}}{\partial x_m}\right)\delta_{ij}-\tilde{\mu}_p\left(\frac{\partial\widetilde{U}_{p,i}}{\partial x_j}+\frac{\partial\widetilde{U}_{p,j}}{\partial x_i}-\frac{2}{3}\frac{\partial\widetilde{U}_{p,m}}{\partial x_m}\delta_{ij}\right) \tag{B.9}$$

$$\begin{aligned}\Sigma^{sgs}_{p,ij}=&\left(\overline{P}_p-\overline{\lambda_p\frac{\partial U_{p,m}}{\partial x_m}}\right)\delta_{ij}-\overline{\mu_p\left(\frac{\partial U_{p,i}}{\partial x_j}+\frac{\partial U_{p,j}}{\partial x_i}-\frac{2}{3}\frac{\partial U_{p,m}}{\partial x_m}\delta_{ij}\right)}\\&-\widetilde{\Sigma}_{p,ij}\end{aligned} \tag{B.10}$$

with

$$\widetilde{P}_p=\bar{\alpha}_p\rho_p[1+2\bar{\alpha}_p\bar{g}_0(1+e_c)]\frac{2}{3}\tilde{q}_p^2 \tag{B.11}$$

$$\tilde{\lambda}_p=\frac{4}{3}\rho_p d_p(1+e_c)\bar{\alpha}_p^2\bar{g}_0\sqrt{\frac{2}{3}\frac{\tilde{q}_p^2}{\pi}} \tag{B.12}$$

$$\tilde{\nu}_p^{kin}=\frac{\tilde{\tau}_p}{2}\frac{2}{3}\tilde{q}_p^2(1+\bar{\alpha}_p\bar{g}_0\Phi_c)\Big/\left[1+\frac{\tilde{\tau}_p}{2}\frac{\sigma_c}{\tilde{\tau}_c}\right] \tag{B.13}$$

$$\tilde{\nu}_p^{coll}=\frac{4}{5}\bar{\alpha}_p\bar{g}_0(1+e_c)\left(\tilde{\nu}_p^{kin}+d_p\sqrt{\frac{2}{3}\frac{\tilde{q}_p^2}{\pi}}\right) \tag{B.14}$$

and the filtered particulate shear viscosity $\tilde{\mu}_p=\bar{\alpha}_p\rho_p\left(\tilde{\nu}_p^{kin}+\tilde{\nu}_p^{coll}\right)$. The filtering procedure can be performed on the transport equation of particle agitation. The filtered transport equation of particle agitation is given by

$$\begin{aligned}\frac{\partial}{\partial t}\bar{\alpha}_p\rho_p\tilde{q}_p^2+\frac{\partial}{\partial x_i}\bar{\alpha}_p\rho_p\widetilde{U}_{p,i}\tilde{q}_p^2=&\frac{\partial}{\partial x_i}\left(\bar{\alpha}_p\rho_p\left(\widetilde{K}_p^{kin}+\widetilde{K}_p^{coll}\right)\frac{\partial\tilde{q}_p^2}{\partial x_i}\right)\\&+\frac{\partial}{\partial x_i}(\rho_p\mathcal{K}_i)-\widetilde{\Sigma}_{p,ij}\frac{\partial\widetilde{U}_{p,i}}{\partial x_j}-\mathcal{S}\\&-\frac{1}{3}(1-e_c^2)\frac{\bar{\alpha}_p\rho_p}{\tilde{\tau}_c}\tilde{q}_p^2-\mathcal{E}-2\\&\times\frac{\bar{\alpha}_p\rho_p}{\tilde{\tau}_p}\tilde{q}_p^2-F+\mathcal{Q}\end{aligned} \tag{B.15}$$

with $\widetilde{K}_p^{kin}$ and $\widetilde{K}_p^{coll}$ the filtered kinematic and collisional diffusivities respectively, given by:

$$\widetilde{K}_p^{kin}=\frac{5}{9}\tilde{\tau}_p\frac{2}{3}\tilde{q}_p^2(1+\bar{\alpha}_p g_0\varphi_c)\Big/\left[1+\frac{5}{9}\tilde{\tau}_p\frac{\xi_c}{\tilde{\tau}_c}\right] \tag{B.16}$$

$$\widetilde{K}_p^{coll}=\bar{\alpha}_p g_0(1+e_c)\left[\frac{6}{5}\widetilde{K}_p^{kin}+\frac{4}{3}d_p\sqrt{\frac{2}{3}\frac{\tilde{q}_p^2}{\pi}}\right] \tag{B.17}$$

$\tilde{\Sigma}_{p,ij}\frac{\partial\widetilde{U}_{p,i}}{\partial x_j}$ is the production of filtered particle agitation by the filtered particle velocity gradient. The terms $\mathcal{K}_i$, $\mathcal{S}$, $\mathcal{E}$, $\mathcal{F}$ and $\mathcal{Q}$ are sub-grid contributions and are defined by the following relations:

$$\mathcal{K}_i=\overline{\alpha_p\left(K_p^{kin}+K_p^{coll}\right)\frac{\partial q_p^2}{\partial x_i}}-\bar{\alpha}_p\left(\widetilde{K}_p^{kin}+\widetilde{K}_p^{coll}\right)\frac{\partial\tilde{q}_p^2}{\partial x_i} \tag{B.18}$$

$$\mathcal{S}=\overline{\Sigma_{p,ij}\frac{\partial U_{p,j}}{\partial x_i}}-\widetilde{\Sigma}_{p,ij}\frac{\partial\widetilde{U}_{p,j}}{\partial x_i} \tag{B.19}$$

$$\mathcal{E}=\frac{1}{3}(1-e_c^2)\rho_p\left[\overline{\frac{\alpha_p}{\tau_c}q_p^2}-\frac{\bar{\alpha}_p}{\tilde{\tau}_c}\tilde{q}_p^2\right] \tag{B.20}$$

$$\mathcal{F}=2\rho_p\left[\overline{\frac{\alpha_p}{\tau_p}q_p^2}-\frac{\bar{\alpha}_p}{\tilde{\tau}_p}\tilde{q}_p^2\right] \tag{B.21}$$

$$\mathcal{Q}=-\frac{\partial}{\partial x_i}\bar{\alpha}_p\rho_p\left(\widetilde{q_p^2U_{p,i}}-\tilde{q}_p^2\widetilde{U}_{p,i}\right) \tag{B.22}$$

Appendix C. Dynamic adjustment of the model constant $K_{\beta\beta}$

Parmentier et al. (2012) proposed adjusting the model constants $K_{\beta\beta}$ dynamically by using a method adapted from Germano et al. (1991) and Lilly (1992). The constant are dependent on both the case simulated and the direction. The idea is to estimate values of $K_{\beta\beta}$ for each cell during the simulation on a coarse grid, by performing a filtering operation of variables over cells in the neighbourhood. Test-level filtered function $\widehat{\bar{f}}$ can be averaged over the base level function $\bar{f}$ for a uniform 3D mesh

$$\begin{aligned}\widehat{\bar{f}}(\mathbf{x},t)=&\frac{1}{7}(\bar{f}(\mathbf{x},t)+\bar{f}(\mathbf{x}+\widehat{\Delta}\mathbf{e}_\mathbf{x},t)+\bar{f}(\mathbf{x}-\widehat{\Delta}\mathbf{e}_\mathbf{x},t)+\bar{f}(\mathbf{x}+\widehat{\Delta}\mathbf{e}_\mathbf{y},t)\\&+\bar{f}(\mathbf{x}-\widehat{\Delta}\mathbf{e}_\mathbf{y},t)+\bar{f}(\mathbf{x}+\widehat{\Delta}\mathbf{e}_\mathbf{z},t)+\bar{f}(\mathbf{x}-\widehat{\Delta}\mathbf{e}_\mathbf{z},t))\end{aligned} \tag{C.1}$$

where $\widehat{\Delta}$ is the test-level filter width. Parmentier et al. (2012) tested the function $g(\Delta^*,\bar{\alpha}_p)$ at the test and the base filter levels. They state that both functions are nearly independent of the choice of the filter width. The model at the base level is given by:

$$\begin{aligned}\bar{\alpha}_p\widetilde{V}_{d,\beta}=&\overline{\alpha_p(U_{g,\beta}-U_{p,\beta})}-\bar{\alpha}_p(\widetilde{U}_{g,\beta}-\widetilde{U}_{p,\beta})\\=&K_{\beta\beta}f(\Delta^*)h(\bar{\alpha}_p)\bar{\alpha}_p(\widetilde{U}_{g,\beta}-\widetilde{U}_{p,\beta})\end{aligned} \tag{C.2}$$

Consequently, one can define the sub-grid drift velocity $\mathcal{T}_\beta$ at test scale as

$$\mathcal{T}_\beta = \widehat{\overline{\alpha_p(U_{g,\beta} - U_{p,\beta})}} - \hat{\bar{\alpha}}_p(\hat{\widetilde{U}}_{g,\beta} - \hat{\widetilde{U}}_{p,\beta}) \tag{C.3}$$

The difference between the sub-grid drift velocity at the test scale and the filtered sub-grid drift velocity $\widehat{\bar{\alpha}_p \widetilde{V}_{d,\beta}} = \widehat{\overline{\alpha_p(U_{g,\beta} - U_{p,\beta})}} - \widehat{\bar{\alpha}_p(\widetilde{U}_{g,\beta} - \widetilde{U}_{p,\beta})}$ is

$$\mathcal{L}_\beta = \mathcal{T}_\beta - \widehat{\bar{\alpha}_p \widetilde{V}_{d,\beta}} = \bar{\alpha}_p(\widehat{\widetilde{U}_{g,\beta} - \widetilde{U}_{p,\beta}}) - \hat{\bar{\alpha}}_p(\hat{\widetilde{U}}_{g,\beta} - \hat{\widetilde{U}}_{p,\beta}) \tag{C.4}$$

$\mathcal{T}_\beta$ at scale $\widehat{\Delta}$ is given by

$$\mathcal{T}_\beta = K_{\beta\beta} f(\widehat{\Delta}) h(\hat{\bar{\alpha}}_p) \hat{\bar{\alpha}}_p(\hat{\widetilde{U}}_{g,\beta} - \hat{\widetilde{U}}_{p,\beta}) \tag{C.5}$$

$\widehat{\bar{\alpha}_p \widetilde{V}_{d,\beta}}$ is calculated by

$$\widehat{\bar{\alpha}_p \widetilde{V}_{d,\beta}} = K_{\beta\beta} f(\Delta^*) h(\bar{\alpha}_p) \widehat{\bar{\alpha}_p(\widetilde{U}_{g,\beta} - \widetilde{U}_{p,\beta})} \tag{C.6}$$

Substitution of these expressions into Eq. (C.4) leads to the following relations:

$$\mathcal{L}_\beta \approx K_{\beta\beta} \mathcal{M}_\beta \tag{C.7}$$

where $\mathcal{M}_\beta = f(\widehat{\Delta}) h(\hat{\bar{\alpha}}_p) \hat{\bar{\alpha}}_p(\hat{\widetilde{U}}_{g,\beta} - \hat{\widetilde{U}}_{p,\beta}) - f(\Delta^*) h(\bar{\alpha}_p) \widehat{\bar{\alpha}_p(\widetilde{U}_{g,\beta} - \widetilde{U}_{p,\beta})}$. We assume that the scale variance of $K_{\beta\beta}$ is negligible at two different scale levels. Thus, we can obtain a model coefficient as

$$K_{\beta\beta} \approx \frac{\mathcal{L}_\beta}{\mathcal{M}_\beta} \tag{C.8}$$

To avoid numerically unstable values of $K_{\beta\beta}$, we calculate the domain-averaged model coefficient along the mean flow as follows:

$$K_{\beta\beta} \approx \frac{\langle \mathcal{L}_\beta \mathcal{M}_\beta \rangle}{\langle \mathcal{M}_\beta \mathcal{M}_\beta \rangle} \tag{C.9}$$

For three-dimensional simulations, the model coefficients along the longitudinal and transverse directions are assumed to be the same and given by following relation:

$$K_{ll} = K_{tt} = \frac{\langle \mathcal{L}_l \mathcal{M}_l + \mathcal{L}_t \mathcal{M}_t \rangle}{\langle \mathcal{M}_l^2 + \mathcal{M}_t^2 \rangle} \tag{C.10}$$

C.1. Dynamic procedure for Mixed model

In order to obtain an expression for $K_{\beta\beta}$, a similar procedure to the one given for the dynamic functional model can be performed. $\mathcal{T}_\beta$ can be defined at test scale as

$$\mathcal{T}_\beta = \frac{\widehat{\Delta}^2}{12} \frac{\partial \hat{\bar{\alpha}}_p}{\partial x_j} \frac{\partial \hat{\widetilde{U}}_{g,\beta}}{\partial x_j} + K_{\beta\beta} f(\widehat{\Delta}) h(\hat{\bar{\alpha}}_p) \hat{\bar{\alpha}}_p(\hat{\widetilde{U}}_{g,\beta} - \hat{\widetilde{U}}_{p,\beta}) \tag{C.11}$$

The difference between the test and filtered scales is

$$\mathcal{L}_\beta = \mathcal{T}_\beta - \widehat{\bar{\alpha}_p \widetilde{V}_{d,\beta}} = \bar{\alpha}_p(\widehat{\widetilde{U}_{g,\beta} - \widetilde{U}_{p,\beta}}) - \hat{\bar{\alpha}}_p(\hat{\widetilde{U}}_{g,\beta} - \hat{\widetilde{U}}_{p,\beta}) \tag{C.12}$$

$\widehat{\bar{\alpha}_p \widetilde{V}_{d,\beta}}$ is calculated by

$$\widehat{\bar{\alpha}_p \widetilde{V}_{d,\beta}} = \frac{\widehat{\Delta}^2}{12} \widehat{\frac{\partial \bar{\alpha}_p}{\partial x_j} \frac{\partial \widetilde{U}_{g,\beta}}{\partial x_j}} + K_{\beta\beta} f(\Delta^*) h(\bar{\alpha}_p) \widehat{\bar{\alpha}_p(\widetilde{U}_{g,\beta} - \widetilde{U}_{p,\beta})} \tag{C.13}$$

Substitution of these expressions into Eq. (C.12) leads to $\mathcal{L}_\beta \approx \mathcal{H}_\beta + K_{\beta\beta} \mathcal{M}_\beta$ where

$$\mathcal{M}_\beta = -f(\widehat{\Delta}) h(\hat{\bar{\alpha}}_p) \hat{\bar{\alpha}}_p(\hat{\widetilde{U}}_{g,\beta} - \hat{\widetilde{U}}_{p,\beta}) + f(\Delta^*) h(\bar{\alpha}_p) \widehat{\bar{\alpha}_p(\widetilde{U}_{g,\beta} - \widetilde{U}_{p,\beta})} \tag{C.14}$$

and

$$\mathcal{H}_\beta = \frac{\widehat{\Delta}^2}{12} \frac{\partial \hat{\bar{\alpha}}_p}{\partial x_j} \frac{\partial \hat{\widetilde{U}}_{g,\beta}}{\partial x_j} - \frac{\overline{\Delta}^2}{12} \frac{\partial \bar{\alpha}_p}{\partial x_j} \widehat{\frac{\partial \widetilde{U}_{g,\beta}}{\partial x_j}} \tag{C.15}$$

We assume that the scale variance of $K_{\beta\beta}$ is negligible at two different scale levels. Thus, the model coefficient is given by

$$K_{\beta\beta} = \frac{\langle (\mathcal{L}_\beta - \mathcal{H}_\beta) \mathcal{M}_\beta \rangle}{\langle \mathcal{M}_\beta \mathcal{M}_\beta \rangle} \tag{C.16}$$

The model coefficients along the longitudinal and transverse directions are given by Eq. (C.10).

Appendix D. Derivation of the Gradient and Full Tensor models

The Gradient and Full Tensor models can be derived from the Taylor series expansion for a variable ϕ,

$$\phi(\boldsymbol{x}) = \phi(\boldsymbol{x}_0) + \frac{\partial \phi}{\partial x_j}(\boldsymbol{x}_0) I_j + \frac{1}{2} \frac{\partial^2 \phi}{\partial x_j x_k}(\boldsymbol{x}_0) I_{jk} + \mathcal{O}(\overline{\Delta}^3) \tag{D.1}$$

where $I_j = (x_j - x_{j_0})$ and $I_{jk} = (x_j - x_{j_0})(x_k - x_{k_0})$. Performing filtering on this expansion gives

$$\bar{\phi}(\boldsymbol{x}) = \phi(\boldsymbol{x}_0) + \frac{\partial \phi}{\partial x_j}(\boldsymbol{x}_0) \bar{I}_j + \frac{1}{2} \frac{\partial^2 \phi}{\partial x_j x_k}(\boldsymbol{x}_0) \bar{I}_{jk} + \mathcal{O}(\overline{\Delta}^3) \tag{D.2}$$

Multiplying the series expansions for the scalar, ϕ, and the vector, λ_i, then filtering yields

$$\begin{aligned} \overline{\phi\lambda_i}(\boldsymbol{x}) = {} & \phi(\boldsymbol{x}_0)\lambda_i(\boldsymbol{x}_0) + \left[\phi(\boldsymbol{x}_0) \frac{\partial \lambda_i(\boldsymbol{x}_0)}{\partial x_j} + \lambda_i(\boldsymbol{x}_0) \frac{\partial \phi(\boldsymbol{x}_0)}{\partial x_j}\right] \bar{I}_j \\ & + \left\{ \frac{1}{2} \left[\phi(\boldsymbol{x}_0) \frac{\partial^2 \lambda_i(\boldsymbol{x}_0)}{\partial x_j \partial x_k} + \lambda_i(\boldsymbol{x}_0) \frac{\partial^2 \phi(\boldsymbol{x}_0)}{\partial x_j \partial x_k}\right] \right. \qquad \text{(D.3)} \\ & \left. + \frac{\partial \phi}{\partial x_j}(\boldsymbol{x}_0) \frac{\partial \lambda_i}{\partial x_k}(\boldsymbol{x}_0) \right\} \bar{I}_{jk} \qquad \text{(D.4)} \end{aligned}$$

Multiplying the series expansion for the scalar, $\bar{\phi}$, and the vector, $\bar{\lambda}_i$, leads

$$\begin{aligned} \overline{\phi\lambda_i}(\boldsymbol{x}) = {} & \phi(\boldsymbol{x}_0)\lambda_i(\boldsymbol{x}_0) + \phi(\boldsymbol{x}_0) \frac{\partial \lambda_i(\boldsymbol{x}_0)}{\partial x_l} \bar{I}_l + \phi(\boldsymbol{x}_0) \frac{\partial^2 \lambda_i(\boldsymbol{x}_0)}{\partial x_l \partial x_m} \bar{I}_l \bar{I}_m \\ & + \frac{\partial \phi}{\partial x_j}(\boldsymbol{x}_0)\lambda_i(\boldsymbol{x}_0) \bar{I}_j + \frac{\partial \phi}{\partial x_j}(\boldsymbol{x}_0) \frac{\partial \lambda_i(\boldsymbol{x}_0)}{\partial x_l} \bar{I}_j \bar{I}_l + \frac{\partial \phi}{\partial x_j}(\boldsymbol{x}_0) \\ & \times \frac{\partial^2 \lambda_i(\boldsymbol{x}_0)}{\partial x_l \partial x_m} \bar{I}_j \bar{I}_l \bar{I}_m + \frac{\partial^2 \phi(\boldsymbol{x}_0)}{\partial x_j \partial x_k} \lambda_i(\boldsymbol{x}_0) \bar{I}_j \bar{I}_k + \frac{\partial^2 \phi(\boldsymbol{x}_0)}{\partial x_j \partial x_k} \\ & \times \frac{\partial \lambda_i(\boldsymbol{x}_0)}{\partial x_l} \bar{I}_j \bar{I}_k \bar{I}_l + \frac{\partial^2 \phi(\boldsymbol{x}_0)}{\partial x_j \partial x_k} \frac{\partial^2 \lambda_i(\boldsymbol{x}_0)}{\partial x_l \partial x_m} \bar{I}_j \bar{I}_k \bar{I}_l \bar{I}_m \end{aligned} \tag{D.5}$$

The series expansion of the particle volume fraction, α_p, is

$$\bar{\alpha}_p(\boldsymbol{x}) = \alpha_p(\boldsymbol{x}_0) + \frac{\partial \alpha_p}{\partial x_j}(\boldsymbol{x}_0) \bar{I}_j + \frac{1}{2} \frac{\partial^2 \alpha_p}{\partial x_j x_k}(\boldsymbol{x}_0) \bar{I}_{jk} \tag{D.6}$$

The series expansion of the filtered gas velocity, $\widetilde{U}_{g,i}$, by replacing the unweighted filtering with Favre-filtering is given as

$$\widetilde{U}_{g,i}(\boldsymbol{x}) = \widetilde{U}_{g,i}(\boldsymbol{x}_0) + \frac{\partial \widetilde{U}_{g,i}}{\partial x_l}(\boldsymbol{x}_0) \widetilde{I}_l + \frac{1}{2} \frac{\partial^2 \widetilde{U}_{g,i}}{\partial x_l x_m}(\boldsymbol{x}_0) \widetilde{I}_{lm} \tag{D.7}$$

The filtering of the multiplication of the particle volume fraction and gas velocity is

$$\begin{aligned} \overline{\alpha_p U_{g,i}}(\boldsymbol{x}) = {} & \alpha_p(\boldsymbol{x}_0) U_{g,i}(\boldsymbol{x}_0) \\ & + \left[\alpha_p(\boldsymbol{x}_0) \frac{\partial U_{g,i}(\boldsymbol{x}_0)}{\partial x_j} + U_{g,i}(\boldsymbol{x}_0) \frac{\partial \alpha_p(\boldsymbol{x}_0)}{\partial x_j}\right] \bar{I}_j \\ & + \frac{1}{2} \left[\alpha_p(\boldsymbol{x}_0) \frac{\partial^2 U_{g,i}(\boldsymbol{x}_0)}{\partial x_j \partial x_k} + U_{g,i}(\boldsymbol{x}_0) \frac{\partial^2 \alpha_p(\boldsymbol{x}_0)}{\partial x_j \partial x_k}\right] \bar{I}_{jk} \\ & + \frac{\partial \alpha_p}{\partial x_j}(\boldsymbol{x}_0) \frac{\partial U_{g,i}}{\partial x_j}(\boldsymbol{x}_0) \bar{I}_{jk} \end{aligned} \tag{D.8}$$

The general model for the sub-grid drift flux, $\bar{\alpha}_p \widetilde{V}_{d,i} = \overline{\alpha_p U_{g,i}} - \bar{\alpha}_p \widetilde{U}_{g,i}$, can be obtained by the subtraction of the multiplication of Eqs. (D.6) and (D.7) from Eq. (D.8) as

$$\bar{\alpha}_p \widetilde{V}_{d,i} = \frac{1}{2}\alpha_p \frac{\partial^2 U_{g,i}}{\partial x_j \partial x_k} \bar{I}_{jk} - \frac{1}{2}\alpha_p \frac{\partial^2 U_{g,i}}{\partial x_l \partial x_m} \widetilde{I}_{lm} + \frac{\partial \alpha_p}{\partial x_j} \frac{\partial U_{g,i}}{\partial x_k} \bar{I}_{jk} - \frac{1}{4} \times \frac{\partial^2 \alpha_p}{\partial x_j \partial x_k} \frac{\partial^2 U_{g,i}}{\partial x_l \partial x_m} \bar{I}_{kl} \widetilde{I}_{lm} \quad \text{(D.9)}$$

with $\bar{I}_k = 0$ if x_0 is the centroid of the filtering volume. By following Okong'o and Bellan (2004), we assume $\bar{I}_j \simeq \widetilde{I}_j$ and $\bar{I}_{jk} \simeq \widetilde{I}_{jk}$. For a cubic top-hat filter, $\bar{I}_{jk}$ is equal to $\overline{\Delta}^2 \delta_{jk}/12$ leading to

$$\bar{\alpha}_p \widetilde{V}_{d,i} = \frac{\overline{\Delta}^2}{12} \frac{\partial \alpha_p}{\partial x_j} \frac{\partial U_{g,i}}{\partial x_j} - \frac{\overline{\Delta}^4}{576} \frac{\partial^2 \alpha_p}{\partial x_j \partial x_k} \frac{\partial^2 U_{g,i}}{\partial x_j \partial x_k} \quad \text{(D.10)}$$

References

Agrawal, K., Loezos, P., Syamlal, M., Sundaresan, S., 2001. The role of meso-scale structures in rapid gas–solid flows. J. Fluid Mech. 445, 151–185.

Anderson, T.B., Jackson, R., 1967. Fluid mechanical description of fluidized beds. Equations of motion. Ind. Eng. Chem. Fund. 6, 527–539.

Anderson, T.B., Jackson, R., 1968. Fluid mechanical description of fluidized beds. Stability of state of uniform fluidization. Ind. Eng. Chem. Fund. 7, 12–21.

Andrews, A.I., Loezos, P.N., Sundaresan, S., 2005. Coarse-grid simulation of gas–particle flows in vertical risers. Ind. Eng. Chem. Res. 44, 6022–6037.

Balzer, G., Boelle, A., Simonin, O., 1995. Eulerian gas-solid flow modelling of dense fluidized bed. FLUIDIZATION VIII, Proc. International Symposium of the Engineering Foundation, J.F. Large and C. Laguérie (Editors), published in 1996 by Engineering Foundation, pp. 409–418.

Bardina, J., Ferziger, J.H., Reynolds, W.C., 1983. Improved Turbulence Models based on Large Eddy Simulation of Homogeneous, Incompressible Turbulent Flows. Technical Report. Rep. TF-19, Dept. of Mech. Engng, Stanford University, Stanford, CA.

Boëlle, A., Balzer, G., Simonin, O., 1995. Second-order prediction of the particle-phase stress tensor of inelastic spheres in simple shear dense suspensions. In: Proc. 6th Int. Symp. on Gas–Solid Flows, ASME FED, pp. 9–18.

Boemer, A., Qi, H., Hannes, J., Renz, U., 1994. Modelling of solids circulation in a fluidized bed with Eulerian approach. In: Avidan, A. (Ed.), Circulating Fluidized Bed Technology. IV. Proceedings of the Fourth International Conference on Circulating Fluidized Beds.

Clark, R.A., Ferziger, J.H., Reynolds, W.C., 1979. Evaluation of Subgrid-scale Models Using an Accurately Simulated Turbulent Flow. Technical Report, Standford University TF-19 5/83 91, pp. 1–16.

Dasgupta, S., Jackson, R., Sundaresan, S., 1994. Turbulent gas–particle flow in vertical risers. AIChE J. 40, 215–228.

De Wilde, J., 2005. Reformulating and quantifying the generalized added mass in filtered gas–solid flow models. Phys. Fluids 17, 113304.

Erlebacher, G., Hussaini, M.Y., Speziale, C.G., Zang, T.A., 1992. Toward the large-eddy simulation of compressible turbulent flows. J. Fluid Mech. 238, 155–185.

Eyink, G.L., 2006. Multi-Scale gradient expansion of the turbulent stress tensor. J. Fluid Mech. 549, 159–190.

Gao, J., Chang, J., Xu, C., Lan, X., Yang, Y., 2008. CFD simulation of gas solid flow in FCC strippers. Chem. Eng. Sci. 63, 1827–1841.

Germano, M., 1986. A proposal for a redefinition of the turbulent stresses in the filtered Navier–Stokes equations. Phys. Fluids 29, 2323.

Germano, M., Piomelli, U., Moin, P., Cabot, W.H., 1991. A dynamic subgrid-scale eddy viscosity model. Phys. Fluids A: Fluid Dynam. 3, 1760.

Gidaspow, D., 1994. Multiphase Flow and Fluidization. Academic.

Gidaspow, D., Jung, J., Singh, R.K., 2004. Hydrodynamics of fluidization using kinetic theory: an emerging paradigm: 2002 Flour-Daniel lecture. Powder Technol. 148, 123–141.

Gobin, A., Neau, H., Simonin, O., Llinas, J.R., Reiling, V., Selo, J.L., 2003. Fluid dynamic numerical simulation of a gas phase polymerization reactor. Int. J. Numer. Methods Fluids 43, 1199–1220.

Heynderickx, G.J., Das, A.K., Wilde, J.D., Marin, G.B., 2004. Effect of clustering on gas–solid drag in dilute flows. Ind. Eng. Chem. Res. 43, 4635–4646.

van der Hoef, M., van Sint Annaland, M., Deen, N., Kuipers, J., 2008. Numerical simulation of dense gas–solid fluidized beds: a multiscale modeling strategy. Annu. Rev. Fluid Mech. 40, 47–70.

Hosseini, S.H., Zivdar, M., Rahimi, R., Samimi, A., 2009. CFD simulation of solid hold-up in gas–solid fluidized bed at high gas velocities. Chemical Product and Process Modeling 4.

Hrenya, C.M., Sinclair, J.L., 1997. Effects of particle-phase turbulence in gas–solid flows. AIChE J. 43, 853–869.

Igci, Y., Andrews, A.T., Sundaresan, S., Pannala, S., O'Brien, T., 2008. Filtered two-fluid models for fluidized gas–particle suspensions. AIChE J. 54, 1431–1448.

Igci, Y., Pannala, S., Benyahia, S., Sundaresan, S., 2012. Validation studies on filtered model equations for gas–particle flows in risers. Ind. Eng. Chem. Res. 51, 2094–2103.

Igci, Y., Sundaresan, S., 2011. Constitutive models for filtered two-fluid models of fluidized gas–particle flows. Ind. Eng. Chem. Res. 50, 13190–13201.

Li, J., Kwauk, M., 1994. Particle-Fluid Two-Phase Flow Energy-Minimization Multi-scale Method. Metallurgical Industry Press, Beijing.

Lilly, D.K., 1992. A proposed modification of the Germano subgrid-scale closure method. Phys. Fluids A: Fluid Dynam. 4, 633.

Liu, S., Meneveau, C., Katz, J., 1994. On the properties of similarity subgrid-scale models as deduced from measurements in a turbulent jet. J. Fluid Mech. 275, 83–119.

McKeen, T., Pugsley, T., 2003. Simulation and experimental validation of a freely bubbling bed of FCC catalyst. Powder Technol. 129, 139–152.

Moreau, M., Simonin, O., Bédat, B., 2009. Development of gas–particle Euler–Euler LES approach: a priori analysis of particle sub-grid models in homogeneous isotropic turbulence. Flow Turbul. Combust. 84, 295–324.

Neau, H., Laviéville, J., Simonin, O., 2010. NEPTUNE_CFD high parallel computing performances for particle-laden reactive flows computational techniques for multiphase flows. In: 7th International Conference on Multiphase Flow – ICMF 2010 Proceedings, International Conference on Multiphase Flow (ICMF).

O'Brien, T.J., Syamlal, M., 1993. Particle cluster effects in the numerical simulation of a circulating fluidized bed. In: Avidan, A.A. (Ed.), Circulating Fluidized Bed Technology. IV. Proceedings of the Fourth International Conference on Circulating Fluidized Beds.

Okong'o, N.A., Bellan, J., 2004. Consistent large-eddy simulation of a temporal mixing layer laden with evaporating drops. Part 1. Direct numerical simulation, formulation and a priori analysis.. J. Fluid Mech. 499, 1–47.

Ozel, A., Parmentier, J.F., Simonin, O., Fede, P., 2010. A priori test of effective drag modeling for filtered two-fluid model simulation of circulating and dense gas–solid fluidized beds. iIn: 7th International Conference on Multiphase Flow – ICMF 2010 Proceedings, International Conference on Multiphase Flow (ICMF).

Parmentier, J.-F., Simonin, O., Delsart, O., 2008. A numerical study of fluidization behavior of Geldart B, A/B and A particles using Eulerian multifluid modeling approach. In: Werther, J., Wirth, K.E., Nowak, W. (Eds.), Ninth International Conference on Circulating Fluidized Beds, Hamburg, Germany.

Parmentier, J.F., Simonin, O., Delsart, O., 2012. A functional subgrid drift velocity model for filtered drag prediction in dense fluidized bed. AIChE J. 58, 1084–1098.

Sagaut, P., 2004. Large Eddy Simulation for Incompressible Flows, second ed. Springer.

Smagorinsky, J., 1963. General circulation experiments with the primitive equations. Mon. Weather Rev. 91, 99–164.

Sundaresan, S., 2000. Modeling the hydrodynamics of multiphase flow reactors: current status and challenges. AIChE J. 46, 1102–1105.

Vreman, B., Geurts, B., Kuerten, H., 1996. Large-eddy simulation of the temporal mixing layer using the clark model. Theoret. Comput. Fluid Dynam. 8, 309–324.

Wang, J., 2009. A review of Eulerian simulation of Geldart A particles in gas-fluidized beds. Ind. Eng. Chem. Res. 48, 5567–5577.

Wang, J., van der Hoef, M., Kuipers, J., 2009. Why the two-fluid model fails to predict the bed expansion characteristics of Geldart A particles in gas-fluidized beds: a tentative answer. Chem. Eng. Sci. 64, 622–625.

Wang, W., Li, J., 2007. Simulation of gas–solid two-phase flow by a multi-scale CFD approach—of the EMMS model to the sub-grid level. Chem. Eng. Sci. 62, 208–231.

Weinstein, H., N., S., Wasserzug, L., 1984. Radial solid density in vertical gas–solid contact systems. AIChE Symp. Ser. 80, 117.

Wen, C.Y., Yu, Y.H., 1966. Mechanics of fluidization. Chem. Eng. Prog. Symp. Ser. 62, 100–111.

Yang, N., Wang, W., Ge, W., Li, J., 2003. CFD simulation of concurrent-up gas–solid flow in circulating fluidized beds with structure-dependent drag coefficient. Chem. Eng. J. 96, 71–80.

Yoshizawa, A., 1986. Statistical theory for compressible turbulent shear flows, with the application to subgrid modeling. Phys. Fluids 29, 2152.

Zang, T.A., Dahlburg, R.B., Dahlburg, J.P., 1991. Direct and Large-Eddy Simulations of Three-Dimensional Compressible Navier–Stokes Turbulence. Technical Report. Interim Rept., Naval Research Lab., Washington, DC.

Zhang, D.Z., VanderHeyden, W.B., 2002. The effects of mesoscale structures on the macroscopic momentum equations for two-phase flows. Int. J. Multiphase Flow 28, 805–822.

Zimmermann, S., Taghipour, F., 2005. CFD modeling of the hydrodynamics and reaction kinetics of FCC fluidized-bed reactors. Ind. Eng. Chem. Res. 44, 9818–9827.